A modular encapsulation system for precision delivery of proteins, nucleic acids and therapeutics

T. D. Luong[1], N. Martel[1], J. Rae[1], H. P. Lo[1], Y-W. Lim[1], Y. Wu[1], K-A. McMahon[1], N. Fletcher[3], K. Thurecht[3], A.P.R. Johnston[4], N. Ariotti[1], T. E. Hall[1*#], and R.G. Parton[1,2*#].

Institute for Molecular Bioscience[1], Centre for Microscopy and Microanalysis[2], Australian Institute for Bioengineering and Nanotechnology[3], The University of Queensland, St Lucia, QLD, 4072, Australia; Monash Institute of Pharmaceutical Sciences[4], Monash University, Parkville, VIC, Australia.

*Correspondence to: thomas.hall@imb.uq.edu.au, r.parton@imb.uq.edu.au

#Equal contribution.

Abstract

Targeted nanoparticles have the potential to revolutionize therapeutics for medical applications. Here, we demonstrate the utility of a flexible precision nanovesicle delivery system for functional delivery of DNA, RNA, proteins and drugs into target cells. Nanovesicles generated by the membrane sculpting protein caveolin, termed caveospheres, can be loaded with RNA, DNA, proteins or drugs post-synthesis or incorporate genetically-encoded cargo proteins during production without the need for protein purification. Functionalized fluorescently-labeled caveospheres form a modular system that shows high stability in biological fluids, specific uptake by target-positive cells, and can deliver proteins, drugs, DNA, and mRNA directly to the cytoplasm and nuclei of only the target cells. We demonstrate their application as a targeted transfection system for cells in culture, as a system to study endosomal escape, and critically, their efficacy in precision tumor killing *in vivo*.

Main

Targeted delivery in nanomedicine is crucial for maximizing therapeutic efficacy by minimizing off-target impacts and minimizing potential side-effects. Techniques for nanoparticle synthesis and their subsequent functionalization by ligand conjugation often require complex manufacturing processes (Muro, 2012; Rosenblum et al., 2018). In the case of antibody-based targeting, binding to the synthesized nanoparticle can be inefficient due to the presence of multiple functional groups on the antibody resulting in heterogeneous orientations (Friedman, Claypool, & Liu, 2013). In complex diseases, like cancer, diverse therapeutic molecules targeting multiple aspects of cancer biology are necessary. Relying solely on a single receptor or pathway can lead to the expansion of drug-resistant cancer cells (Kedmi et al., 2018). This obviates the need for a platform of flexible and versatile yet specific targeted vehicles that can deliver therapeutic molecules to a variety of different cancer cell types. An ideal system would be one that allows for multiple treatment strategies including chemotherapies, immunotherapies, and RNA therapies.

We have developed a modular nanovesicle system based on expression of the mammalian caveolin-1 protein (hereby termed caveolin) in a bacterial host. Caveolin is incorporated into the cytoplasmic membrane of *E.coli* and where it oligomerizes to induce curvature and drive inward vesicle formation ((Walser et al., 2012); Fig. S1a). The resulting nanovesicles (termed caveospheres), of approximately 50nm diameter (Fig. S1b), accumulate to an extremely high density within the cytoplasm of the bacteria and can be purified with high yield. Each caveosphere contains approximately 150 caveolin molecules arranged as disc-like oligomers occupying the cytoplasmic leaflet of the vesicles as shown by cryoelectron microscopy (Porta et al., 2022), and a precisely defined lipid composition. Bacterial proteins are largely excluded from these nanovesicles (Walser et al., 2012). This structurally-defined and genetically-encoded system allows functional modification of the caveolin fusion proteins. Moieties with defined roles (e.g. antibody-binding, purification) can be attached to both N- and C-termini of the caveolin protein which are both orientated towards the outside of the caveosphere and so are available for interactions with targets (Ariotti et al., 2015).

Here, we demonstrate the ability of the caveosphere system to precisely deliver encapsulated cargoes into the cytoplasm and nucleus of targeted cells whereby they can effectively modulate cellular responses through delivery of their molecular payload.

Specifically, we show i) efficient loading with diverse macromolecules including RNA, DNA, protein and both water-soluble and lipophilic drugs, ii) loaded, functionalized caveospheres can deliver cargo specifically to a variety of different target-positive cells in mixed culture, iii) caveosphere-mediated targeted transfection of RNA or DNA results in high-efficiency, uniform expression in target cells, iv) delivery of fluorescent proteins with organelle-specific tags can used to elucidate key aspects of targeted delivery such as endosomal escape, v) functionalized, far-labelled caveospheres loaded with chemotherapeutics can be specifically targeted to tumours and are able to reduce tumour size in a mouse xenograft model.

Engineering caveospheres for encapsulation of diverse cargoes and cell-specific targeting

We first investigated the possibility of incorporating recombinant proteins into caveospheres as they form by budding into the cytoplasm from the cytoplasmic membrane using a method that avoids cargo protein expression, purification, and encapsulation. We designed a bicistronic vector encoding both the caveosphere-generating fusion protein and the bright fluorescent protein mScarlet (cargo) tagged at the N-terminus with a short periplasmic targeting signal (Fig. 1a). The integration of mScarlet into the caveospheres during formation using this genetically-encoded method (termed GE-caveospheres) was demonstrated by their fluorescence post-purification (Fig. 1b i-ii). TEM analysis showed GE-caveospheres to possess the typical spherical morphology with a diameter of approximately 50 nm, indistinguishable from unloaded caveospheres generated with the original vector (Fig. 1b iii compared to S1b). Ultracentrifugation of the GE-caveospheres resulted in a brightly fluorescent pellet, which was lost with prior detergent treatment (Fig. S2a-b). Encapsulation was further tested by treatment with $CuCl_2$ to quench accessible mScarlet fluorescence. Detergent-treated spheres, but not native spheres, showed quenching of the putative cargo protein (Fig S2c-e).

In sucrose gradients, mScarlet fluorescence cofractionated with the CAV1 protein as detected by Western blotting within the 40-60% sucrose fractions (Fig. 1c i-ii). Cryo-correlative light and transmission electron microscopy (cryoCLEM) of mScarlet loaded GE-caveospheres demonstrated enrichment of the mScarlet fluorescence in areas that correlated with structurally uniform nanovesicles (Fig. 1d). Quantitation of the incorporation of mScarlet into caveospheres showed 0.132 ± 0.018 µg mScarlet (mean ± SD) in 1 mg of GE-

caveospheres (1.018 ± 0.107 mScarlet molecules per caveosphere) (number of particles per 1mg caveosphere by nanoparticle tracking analysis Fig. S1c, standard curve Fig. S4a).

Taken together, these results demonstrate that genetically-encoded proteins that are expressed in the periplasm of the bacteria can be encapsulated into the lumen of forming caveospheres, providing a simple system which bypasses the requirement for cargo protein production and purification.

We next tested physical methods of encapsulation which would allow incorporation of diverse cargoes. We evaluated three distinct methods; freeze-thaw cycling, electroporation, and sonication (Fig. S3a) for encapsulation of EGFP and mScarlet proteins (Fig. 1e & S3c). The association between cargo and caveospheres was tested by ultracentrifugation (Fig. 1f & S3d-e) and negative stain TEM was utilized to evaluate their morphology. All methods demonstrated specific encapsulation of fluorescent proteins while nanovesicle morphology was maintained (Fig. 1f & S3b-e). Sonication was the most effective method of encapsulation, exhibiting the highest level of cargo incorporation while retaining the morphology of unsonicated vesicles as judged by cryoelectron microscopy (Fig. 1g). The highest loading obtained using this method corresponded to approximately 12 molecules of EGFP per 50nm vesicle (12.2 ± 1.29; Fig. S1c, standard curve in Fig. S4b).

Next, we examined the ability of caveospheres to retain their cargo after sonication. EGFP-loaded caveospheres treated at 37°C for 30 min or 1 hour in media with pH from 7.4 to 4.5 retained their contents at neutral pH but released it at lower pH levels (Fig. 1h & S3f), revealing an unexpected pH sensitivity.

As a first step in exploring the potential therapeutic applications of caveospheres as an anti-cancer drug delivery vehicle, we loaded caveospheres with Doxorubicin (DOX), a chemotherapeutic agent associated with significant side-effects including cardiotoxicity (Fornari et al., 1994; Momparler et al., 1976; Tacar, Sriamornsak, & Dass, 2012). As demonstrated for fluorescent proteins, we were also able to achieve specific encapsulation of DOX while preserving nanovesicle morphology (Fig. 1i-k). We next tested the capacity of caveospheres to encapsulate plasmid DNA. Plasmid DNA was fluorescently labeled with

SYBR green and loaded into caveospheres via sonication. Any unincorporated plasmid DNA was then removed by DNAse 1 treatment followed by centrifugal filter purification (Fig. 1l). Again, negative staining by TEM showed that the morphology of the DNA-loaded caveospheres was maintained (Fig. 1m). Encapsulation efficiency was evaluated and quantified using fluorescence. In sonication-loaded spheres, DNA was protected from DNAse1 treatment consistent with encapsulation, whereas DNA incubated in solution with non-sonicated caveospheres was completely cleaved (Fig. 1n-p).

The caveosphere fusion protein contains an IgG binding Z-domain resulting in approximately 150 IgG binding Z-domains per nanovesicle (Walser et al., 2012). This modularity has the potential to enable targeted delivery to specific cells, tissues and disease states, and allow fluorescent labeling for precise tracking. In order to produce an externally-labelled, trackable particle which retains cargo-loading capacity we specifically bound Alexa-488 conjugated rabbit IgG secondary antibodies to the caveosphere surface via Z-domain. We were able to achieve a labelling efficiency of 8.87 ± 0.13 IgG molecules per caveosphere (Fig. 1q & S1c, standard curve shown in Fig S4c). This represents an occupancy of approximately 6% of the 150 theoretical Z-domain epitopes on the caveosphere surface. The *in vivo* application of the caveospheres as a potential trackable therapeutic delivery system necessitates stability in complex biological fluids. Fluorescently-labeled caveospheres incubated in tissue culture media with 10% serum at 37°C for 72 hours showed fluorescence quantitatively indistinguishable from the controls (Fig. 1s-t), indicating that caveospheres retained their surface antibodies during the incubation period.

Caveospheres mediate highly specific targeted transfection

Having efficiently incorporated DNA into caveospheres, we next investigated whether targeted caveospheres can deliver DNA to the cytosol and/or nucleus of target cells. We first double-labelled caveospheres with both Alexa-488 antibodies (for tracking) and anti-EGF-R antibodies (for targeting to the human EGF receptor). We then validated specific targeting and uptake of in EGF-R positive A431 cells in mixed culture with EGF-negative HepG2 cells (Fig S5a-b). We then loaded caveospheres coated with anti-EGFR only with plasmid DNA encoding EGFP.

After incubation in mixed culture for 1 hour, remarkably, specific expression of EGFP occurred exclusively in A431 cells, while HepG2 cells did not show any detectable expression (Fig. 2a-b). We term this process caveosphere-mediated targeted transfection (CmTT). In contrast, delivery of the expression vector by Lipofectamine showed no selectivity and EGFP expression was observed in both A431 and HepG2 cells (Fig. 2a-c). Furthermore, the transfection efficiency, expressed as the percentage of cells transfected, was significantly higher with caveospheres (86.9 ± 2.1%) compared to Lipofectamine (47.5 ± 8.1%) in A431 cells (Fig. 2d). An additional striking difference between the CmTT method and the Lipofectamine method, was the uniformity of EGFP expression between cells in the CmTT group, in contrast to the Lipofectamine transfected cells where expression was highly variable (Fig. 2e). These findings demonstrate two striking advantages of the caveosphere system for transfection; 1) targeted delivery to specific cell types and 2) a greater consistency of expression level over the cell population. Similar results were obtained for functional delivery of mRNA into target A431 cells using the CmTT method. Functionalized mRNA sonication-loaded caveospheres also gave a transfection efficiency higher than Lipofectamine (% cells transfected), and with less variable expression, similar to the results with encapsulated DNA (Fig. S6 a-c).

Next, we explored the potential for decorating caveospheres with genetically encoded binding domains with specificity for cell-surface ligands. We leveraged the high affinity between the receptor-binding domain (RBD) of SARS-CoV-2 virus and the human ACE2 receptor to generate a virus-like particle capable of being selectively endocytosed by bronchial epithelial cells. To this end, we generated a vector encoding which, in addition to the caveosphere fusion protein (MBP-Z-CAV1), also expresses the RBD fused to human Caveolin1 (SARS-CoV-2-RBD-CAV1). This co-expression system generated hybrid spheres containing both the Z-domain and SARS-CoV-2-RBD on the surface (Fig. 2f-g & S5c).

We labelled SARS-CoV2-caveospheres with Alexa-488 antibodies as before, and added to the cultures of the human bronchial epithelial cell line BEAS-2B (Fig. S5d-e). Furthermore, after loading SARS-Cov2-caveospheres with EGFP plasmid, uptake by BEAS-2B cells resulted in uniform expression of EGFP across the culture (Fig. 2h-i). This demonstrates the ability to

transduce target cells using diverse receptor-ligand systems and the potential of the caveosphere system for rapid testing of viral protein-host cell interactions.

The antibody-dependent transfection mediated by the CmTT method offers new possibilities for protein expression in cells such as T-cells that have, to date, been refractory to transfection (Rahimmanesh, Totonchi, & Khanahmad, 2020). We functionalized caveospheres with anti-CD3E and were able to deliver EGFP into a Jurkat cell line with an efficiency of 81.65 ± 0.6%, significantly higher than Lipofectamine (4.6 ± 0.54%). Conversely, when using non-functionalized spheres, no cells were transfected (Fig. S6d-f). This highlights the potential of using caveospheres for delivery to challenging cells, with potential applications in designing and personalizing T-cell therapies (Billingsley et al., 2020; Pinto, Cordeiro, & Faneca, 2023; Rurik et al., 2022).

Finally, we attempted to deliver a DNA cassette with a functional consequence, rather than a benign fluorescent reporter, using caveospheres. We selected DNA encoding diphtheria toxin A (DTA), a highly potent toxin, which must be delivered into the cell cytosol to induce rapid cell death (Dai et al., 2021; Yamaizumi et al., 1978). We used CmTT with EGF-R functionalized caveospheres in mixed cultures of A431 and HepG2 cells in comparison to Lipofectamine-mediated delivery. When using Lipofectamine as a delivery method, cell death occurred indiscriminately in the two cell types (Fig. 2k). In contrast, the CmTT method resulted in almost complete ablation of A431 cells while leaving HepG2 cells unaffected in the same culture milieu (Fig. 2j).

Use of caveospheres as a system to study endosomal escape

Transport of endocytosed particles (such as nanoparticles or caveospheres) into the cytosol and nucleus is limited by a low level of escape from the endosome (Gilleron et al., 2013; Kim et al., 2015; Teo et al., 2021), yet DNA and RNA delivered using the CmTT system results in expression, demonstrating that cargo is able to escape the endosome and reach the cytoplasm. The high selectivity, efficiency and reproducibility of this system offers a unique opportunity to dissect endosomal escape. We used CmTT for a targeted mini-screen to identify reagents that enhance endosomal (or endo-lysosomal) escape, with the rationale that the extent of EGFP fluorescence from a caveosphere-encapsulated DNA reporter would

provide a direct and comparative readout. As proof of principle, we selected a range of lysosomotropic agents (amantadine, azithromycin, chloroquine, dimebon, tamoxifen, amitriptyline, siramesine, UNC10217938A) (Ashfaq et al., 2011; Brock et al., 2019; Heath et al., 2019; Lu et al., 2017; Tian et al., 2021; Yang et al., 2015) and applied them to A431 cells cultured in 96-well plates and pre-incubated for 1.5 hours with anti-EGFR-functionalized caveospheres loaded with an EGFP-plasmid. Chloroquine showed the highest enhancement of EGFP expression (Fig. 3a). Since caveospheres are unstable at low pH (Fig. 1q), we reasoned that treatment with bafilomycin A1, an inhibitor of the proton ATPase (Fedele & Proud, 2020; Klionsky, Nyfeler, & Murphy, 2012; Yamamoto et al., 1998) that attenuates lysosomal acidification, may increase the viability of cargo and produce an additive or synergistic effect on delivery. Indeed, the combination of bafilomycin A1 and chloroquine significantly increased reporter expression level above that seen with chloroquine alone without affecting cell viability (Fig 3b and S7a-c).

Protein expression from an encapsulated plasmid represents a sensitive system to detect endosomal escape due to potential amplification of many orders of magnitude during transcription and translation, particularly when driven by a strong promoter such as CMV. We next investigated whether the CmTT system would allow visualization of a non-amplified fluorescently-tagged protein cargo. We generated and purified 3 proteins for encapsulation; mNeonGreen protein, or mNeonGreen incorporating either an N-terminal nuclear localization signal, NLS, or a nucleolus localization signal, NLS-7R. Nuclear and nucleolar signals ensured that any proteins reaching the cytosol would associate with the nucleus or nucleolus, respectively, allowing unequivocal assessment and quantitation of endosomal escape. NLS-mNeonGreen and NLS7R-mNeonGreen were encapsulated in anti-EGFR spheres using the sonication method (termed functionalized mNeonGreen, NLS-mNG-spheres and NLS7R-mNG-spheres respectively).

A431 cells incubated with functionalized NLS-mNG-spheres and NLS7R-mNG-spheres showed negligible cytoplasmic/nuclear labelling suggesting that any endosomal escape of the fluorescent protein was below the limits of detection (Fig.3). The increased labelling of putative endosomal structures as compared to mNG-spheres without an organelle tag (NLS7R>NLS spheres; Fig. 3c-d) may reflect greater uptake of these spheres due to

residual (membrane-bound non-encapsulated) positively charged protein being present on the surface of the sphere (also see Cupic et al., 2019; Teo et al., 2021). Using the anti-EGFR functionalized NLS7R-mNG-spheres, we then examined whether the lysosomotropic agents that increased plasmid delivery using the CmTT method would result in any detectable endosomal protein escape. Addition of chloroquine alone, but not bafilomycin alone, resulted in a small but significant mNeonGreen signal within the nucleus. When added together bafilomycin and chloroquine showed a strongly synergistic effect with a far greater accumulation of mNeonGreen signal within the nucleus indicating a synergistic enhancement of endosomal escape (Fig. 3e-f).

Tumour targeting and anti-tumour activity of caveospheres in an *in vivo* model

Having demonstrated the stability and targeting capacity of caveospheres in cell culture systems, we investigated their capacity to reach tumor cells *in vivo*. We utilized a well-characterized mouse xenograft model in which an EGFR-positive MDA-MB-468 orthotopic breast cancer cell line is introduced in the left mammary fat pad of a Balb/c nu/nu mouse at 12 weeks of age (Fig. 4a) (Krüwel et al., 2016). Caveospheres (200 µg) functionalized with anti-EGFR and Alexa680 secondary antibody (near-infrared fluorophores used for deeper tissue penetration) were injected intravenously (Ntziachristos, Bremer, & Weissleder, 2003; Pansare et al., 2012; Shi, Wu, & Pan, 2016). After 24 hours, whole animal imaging revealed the specific accumulation of Alexa 680 in the region of the tumor (Fig. 4b). Subsequent imaging of the tumor and specific organs *ex vivo* indicated a significantly higher average radiant efficiency in the tumors from the cohort administered with the anti-EGFR-functionalized caveospheres compared to the cohort given the untargeted spheres (Fig. 4c). Western blot and immunofluorescence staining against CAV1 in histological sections of tumors showed significantly higher levels of caveosphere-derived CAV1 in the targeted caveospheres cohort than the untargeted cohort (Fig. 4d-f). Taken together, these results suggest that antibody labeling of fluorescent caveospheres allows specific targeting to tumors *in vivo*.

Finally, we aimed to test the specificity and efficacy of DOX-loaded caveospheres in the mouse xenograft model. We first tested the DOX-loaded anti-EGFR antibody decorated caveospheres in a cell culture model and showed that they were effective in tumour cell

killing as compared to Free-DOX or DOX-loaded caveospheres (Fig. S8a & 5a-b). BALB/c nude mice were then injected with the anti-EGFR-functionalized DOX-loaded caveospheres, EGFR-functionalized unloaded caveospheres, DOX-loaded caveospheres (without EGFR antibody), Free-DOX, (in the same DOX dose of 4 mg/kg, in 200 µL PBS 1x), and saline (Fig. 5c). The general health of the mice was monitored (weights given in Fig. S8b). We observed a significant decrease in the final tumor volume in mice treated with anti-EGFR-functionalized DOX-loaded caveospheres (48.642 ± 11.1 % of the initial volume) (Fig. 5d), and more effective tumor growth inhibition than in mice treated with Free-DOX or DOX-loaded caveospheres (without EGFR-functionalization) (Fig. 5e-f). Quantification of left-ventricular cardiac wall thickness from histological sections as a measure of cardiotoxicity demonstrated a significant decrease in the free-DOX treated mice compared to those treated with anti-EGFR functionalized DOX loaded spheres and saline only controls (Fig. 5g-h) demonstrating that targeted delivery encapsulated within caveospheres significantly decreased toxic side effects of the administered DOX.

These data demonstrate that DOX-loaded caveospheres can effectively and rapidly enter both cells and solid tumors to deliver their payload, reducing tumor size and minimizing cardiac side-effects.

Conclusions

In this study we have characterized a unique modular nanoparticle vesicle as a system for understanding, and mediating, targeted delivery of encapsulated cargoes. The modular caveosphere system allows labeling with antibodies or genetically encoded peptide binding domains to potentially any surface antigen of interest. Moreover, this endows the spheres with unique targeting and delivery capabilities; targeted caveospheres, but not undecorated spheres, deliver molecules such as DNA, mRNA, proteins, and drugs into the cytosol and nucleus of target cells. The power of the CmTT system is illustrated by functional delivery to only the target cells of interest in a mixed culture system (illustrated by anti-EGFR antibodies for tumor cell targeting), and to cells that are difficult to transduce through other means, such as T-cells targeted through surface CD3E. The ability of CmTT to target specific cell types for efficient delivery of diverse cargoes has great potential for advancing gene

therapy applications. The versatility of the system is demonstrated by utilizing the surface Z-domain not only for targeting purposes but also for specific binding to fluorescent antibodies, enabling simple labeling and tracking of nanoparticles *in vitro* and *in vivo*. The caveosphere can be further engineered to mimic virus particles, with the spike protein of SARS-Cov-2 being used as a proof of principle. The establishment of a simple and rapid system for generation of surrogate viruses that effectively enter human target cells offers potential for early-stage screening of antibodies and other molecules to inhibit virus infection. Furthermore, this ability will enable the rapid incorporation of nanobody therapeutics as new targeting sequences are discovered.

Functional delivery of mRNA, DNA, and proteins specifically to target cells with minimal off-target effects is a powerful feature of the caveosphere system. We have demonstrated that this selectivity translates into precision targeting of tumor cells *in vivo*. While further refinement of the system would be required for *in vivo* applications in view of their bacterial origin (see Caveats in Supplementary 10), this highlights the potential for utilizing caveospheres in chemotherapeutic targeting of cancer cells as well as in imaging and diagnosis. The high specificity of caveospheres in delivering highly toxic molecules to individual target cells while exerting minimal impact on neighboring cells was demonstrated by a reduction of the adverse effects on the heart compared to the non-packaged therapeutic agent.

Finally, the caveosphere system provides a highly reproducible well-characterized system for understanding how a vesicle-packaged cargo can escape the endosome and reach its target location inside a cell. The fluorescently labeled and targeted caveospheres show remarkable stability at 37°C in biological fluids but instability at low pH, a feature of the system that awaits further molecular characterization but which we speculate may allow release of contents within endo/lysosomal compartments. We demonstrate how the system can be used to screen for agents that enhance this process with a simple high fluorescence assay. This gives the potential to dissect the mechanisms involved in the crucial process of endosomal escape both genetically and through drug screening.

Acknowledgments

This work was supported by the National Health and Medical Research Council of Australia grants APP1140064 and APP1150083 to R.G.P. and by the Australian Research Council (Centre of Excellence in Convergent Bio-Nano Science and Technology CE140100036 to R.G.P and A.P.R.J). RGP was supported by an NHMRC fellowship APP1156489 and is now an Australian Research Council (ARC) Laureate Fellow. N.A is supported by a Human Frontiers Science Program Grant (RGP011/2023). The authors acknowledge the use of the Microscopy Australia Research Facility at the Centre for Microscopy and Microanalysis at The University of Queensland.

Author contributions

Conceptualization, R.G.P., T.D.L., A.P.R.J., T.E.H.; methodology, T.D.L., R.G.P., T.E.H., N.M., J.R., N.A., A.P.R.J., N.F; formal analysis, T.D.L., R.G.P., T.E.H., N.M., J.R., N.A., A.P.R.J., N.F; data curation, T.D.L., Y.-W.L.; funding acquisition, R.G.P., A.P.R.J.; supervision, R.G.P., T.E.H., A.P.R.J, K.T.; writing – original draft, R.G.P., T.E.H., T.D.L., H.P.L, Y.W., K.A.M., Y.-W.L.; writing – review & editing, R.G.P., T.E.H., T.D.L., H.P.L, Y.W., K.A.M., Y.-W.L., A.P.R.J., N.F., K.T.; project administration, R.G.P., T.E.H., A.P.R.J.

Declaration of interests

The authors declare no competing interests

Inclusion and diversity

We support inclusive, diverse and equitable conduct of research

Materials and Methods

Cell lines and Culture Conditions

A431 (epidermoid carcinoma, CRL-1555), HepG2 (liver cancer, HB-8065), BEAS-2B (bronchial epithelium, CRL-3588), and Jurkat (T lymphocyte, TIB-152) cells were cultured in their respective media: Dulbecco's Modified Eagle Medium (DMEM, Cat no. 11965092, ThermoFisher Scientific) for A431 and HepG2 cells, a 50:50 mixture of DMEM and Ham's F-12 Nutrient Mix (Cat no. 11765054, ThermoFisher Scientific) for BEAS-2B cells, and RPMI 1640 (Cat no. 11875093, ThermoFisher Scientific) for Jurkat cells. All media were

supplemented with 10% fetal bovine serum (FBS, Hyclone characterized serum, Quantum Scientific, Lot no. KPJ22093) and L-glutamine (200 mM, Cat no. 25030081, ThermoFisher Scientific). The cells were maintained under standard conditions at 37°C in a 5% CO_2 incubator. All cell lines were routinely tested for mycoplasma.

SDS PAGE and Western blot analysis

For SDS-PAGE, caveosphere fractions were denatured with NUPAGE 4x LDS Sample Buffer (Cat no. NP0008, ThermoFisher Scientific) with 10% beta-mercaptoethanol at 95°C for 10 minutes. Proteins were separated on SDS-PAGE gels using Tris-Glycine buffer and were either subjected to Coomassie Blue staining or transferred to an Immobilon-P 0.45 µm PVDF membrane (Cat no. IPVH00010, Merck). The membrane was blocked with 5% skim milk blocking buffer for 1 hour and incubated with a primary antibody overnight. The membrane was then washed with PBST for 10 min three times and incubated with a corresponding secondary antibody (1:5000). The membrane was then washed again with PBST for 10 min three times before visualization of protein bands. Primary antibodies used in this study were rabbit anti-CAV1 (Cat no. 610060, BD Biosciences, 1:5000 dilution), mouse anti-EGFP (Cat no. 11814460001, Roche Diagnostics, 1:5000 dilution), and mouse anti-Actin (Cat no. MAB1501, Merck, 1:5000 dilution) as a loading control. Secondary antibodies for western blotting included Goat anti-Rabbit IgG (H+L) cross-adsorbed secondary antibody, HRP (Cat no. G-21234, Life Technologies, 1:5000 dilution) for rabbit anti-CAV1, and Goat anti-Mouse IgG (H+L) cross-adsorbed secondary antibody, HRP (Cat no. G-21040, Life Technologies, 1:5000 dilution) for anti-EGFP and anti-Actin. Bound IgG was visualized using the Clarity™ Western ECL Substrate (Cat no. 1705061, Bio-Rad). Chemiluminescence was detected using ChemiDoc Imaging System (BIO-RAD). The final images were conducted by merging the chemiluminescence image (showing the WB band) and the colorimetric image (showing the ladder).

Tumor tissue was homogenized using an IKA T10 basic Ultra-Turrax homogenizer. Both tissue and cells were lysed in RIPA buffer containing 50 mM Tris pH 7.5, 150 mM NaCl, 5 mM EDTA pH 8.0, and 1% Triton X-100, supplemented with cOmplete™ mini EDTA-free protease inhibitor cocktail (Cat no. 11836170001, Sigma Aldrich). The lysates were clarified by

centrifugation (17,000*g*) at 4°C. Protein content in the tumor samples was quantified using the Pierce BCA Protein Assay Kit (Cat no. 23225, ThermoFisher Scientific) with bovine serum albumin (BSA) as the standard. Forty micrograms of cellular protein were resolved by 10% SDS-PAGE and transferred to an Immobilon-P 0.45 µm PVDF membrane (Merck). Bound IgG was visualized using horseradish peroxidase-conjugated secondary antibodies and Clarity™ Western ECL Substrate (Cat no. 1705061, Bio-Rad).

Recombinant DNA

Plasmids used in this study were:

- pNMTMA_MBP-Z-Cav1-His6 (Walser et al., 2012, Addgene 223701): to produce **standard caveospheres** containing the anti-IgG Z-domain of protein A. Those caveospheres were used for physical loading cargo, cellular uptake, cell transfection and *in vivo* experiments
- pNMTMA_MBP-Cav1-His6 (Walser et al., 2012, Addgene 223700): to produce caveospheres minus Z-domain (without the Z-domain on surface)
- pNMTMA_MBP-Cav1-H6_Spike_RBD_Cav1 (Addgene 223702): to produce caveospheres decorated with the spike protein from Sars-Cov2 (SARS-Cov-2-caveospheres)
- pNMTMA_MBP_Z_Cav1_H6_Periplasmic_mScarlet (Addgene 223703): to produce caveospheres with periplasmically encapsulated mScarlet (GE-caveospheres)
- pETDuet-mScarlet (Addgene 223704): for production of mScarlet by *E.coli*
- pEGFP-C1 (Clontech): Mammalian expression vector encoding EGFP-C1
- DTA in pCDEST2 (Addgene 223705): Mammalian expression vector encoding Diptheria toxin A
- pOPINE-GFP (Addgene 223706): for production of EGFP by *E.coli*
- pETDuet-mNeonGreen (Addgene 230970): for production of mNG by *E.coli*
- pETDuet-nls-mNeonGreen (Addgene 230971): for production of NLS-mNG by *E.coli*
- pETDuet-nls-7R- mNeonGreen: (Addgene 230972) for production of NLS-7R-mNG by *E.coli*

Caveosphere preparation

Caveospheres were produced as previously described (Walser et al., 2012). Briefly, *E. coli* (Rosetta DE3) carrying caveosphere-expressing plasmids were initially cultured in LB and transferred to Terrific Broth at 37°C. Recombinant CAV1 fusion protein induction and caveosphere formation were achieved by adding 1 mM IPTG (Astral Scientific) to the bacterial medium. Following overnight culture at 37°C, cells were lysed using a cell disruptor (Constant Systems), and cellular debris was removed via centrifugation (15,000*g*, 30 min). Caveospheres were purified using an amylose resin (NEB) column affinity chromatography based on surface protein MBP.

Recombinant protein production

mScarlet, EGFP, mNeongreen, NLS-mNeongreen and NLS-7R-mNeongreen were produced by expression in *E. coli* (Rosetta DE3) overnight followed by TALON® Superflow™ histidine-tagged column affinity chromatography. The proteins were concentrated using Amicon Ultra Centrifugal Filters- 0.5 10 kDa MWCO (Merck Millipore) and frozen at a stock concentration of 8 mg/mL.

Caveosphere quantification

The quantification of produced caveospheres was based on their protein component concentration in solution, determined using the Pierce™ Bicinchoninic Acid Assay Kit (BCA protein assay) (Thermofisher). To analyze the nanoparticles (NPs), 1 mg/mL of protein caveosphere underwent nanoparticle tracking analysis (NTA) utilizing NanoSight NS300. This analysis determined both the number of particles in 1mg/ml protein caveosphere solution and the hydrodynamic diameter distribution of the particles.

Imaging of fluorescence within microcentrifuge tubes

Microcentrifuge tubes were imaged using a ChemiDoc MP Imaging System (BIO-RAD; red channel 605/50 filter, green channel 530/28 filter).

Testing of encapsulation by ultracentrifugation and copper ions

Caveospheres with genetically-encoded mScarlet (GE-caveospheres) were incubated in 1% Triton X-100, 37°C for 1 hour to disrupt the particle membrane. The standard GE-caveospheres and the disrupted GE-caveospheres were centrifuged at 120,000*g* for 2 hours in an TLA-55 Fixed-Angle Rotor of Optima MAX-XP Ultracentrifuge (Beckman coulter)

followed by imaging of fluorescence using a ChemiDoc MP Imaging System as above. To determine the effective concentration for fluorescence quenching by copper ions, different concentrations of $CuCl_2$ (5-0.156 mM) were incubated with free mScarlet (0.1 mg/mL) for 1 hour at room temperature. Then, 1mg/mL of GE-caveospheres, GE-caveosphere treated with Triton X-100 or free mScarlet (0.2 μg/mL) were then mixed with 0.02 mM $CuCl_2$ and incubated for 1 hour at room temperature.

Sucrose gradient analysis of caveospheres

For sucrose gradient analysis, the caveosphere mixture was layered onto a 20%–80% discontinuous sucrose gradient and subjected to velocity gradient centrifugation (120,000*g*, 6 hours, SW 41 Ti Swinging-Bucket Rotor, Beckman Coulter). Twenty fractions were collected from the bottom of the tube, numbered, and transferred to a 96-well plate for western blotting using rabbit anti-CAV1 antibody (BD Bioscience). To determine the presence of GE-caveospheres, fluorescent measurements of all fractions were conducted using a microplate reader as above.

Quantification of fluorescent proteins, antibodies, DNA and doxorubicin using a microplate reader

To quantify fluorescent protein concentration, the linear correlation between fluorescent protein concentration and fluorescent signal was measured using a microplate reader. For mScarlet, the concentration range was 0.575 mg/mL - 1.4×10^{-4} mg/mL (λex 569 nm, λem 594 nm). For EGFP, the range was 1.16 mg/mL - 4.5×10^{-4} mg/mL (λex 488 nm, λem 507 nm). Sample concentrations were calculated using the linear regression equation derived from the standard curves provided in the supplementary information.

For quantification of antibody labeling of caveospheres, the same plate reader methodology was used to establish the linear correlation between concentration of fluorescent antibodies and fluorescent signal (λex – 490 nm and λem – 525 nm). The microgram quantity of antibody binding per mg of caveospheres was calculated using the same methodology based on the fluorescence (λex – 490 nm and λem – 525 nm) and the protein concentration of caveospheres determined by a BCA protein assay as above at the fractions 9-16 (40-60%

sucrose density). Number of antibody molecules per single caveosphere was calculated according to the following equation:

$$\text{number antibodies per single particle} = \frac{\textit{antibody in 1mg of sphere } (\mu g) \times N_A}{10^6 \times 150{,}000 (g/mol) \times 2.62 \times 10^{12}}$$

DNA concentration was measured by establishing the linear correlation between SYBR™ Safe labeled DNA concentration and fluorescence (λex 498 nm, λem 522 nm). Doxorubicin concentration was determined in the same way using fluorescence absorbance at 475 nm.

Electron microscopy of caveospheres

Negative staining was performed by applying 4% uranyl acetate to 12 µL of caveospheres on formvar-coated grids, followed by grid drying and examination under a JEOL 1011 electron microscope at 80kV accelerating voltage. For cryo-electron microscopy, GE-caveospheres were added to R2/2 Quantifoil grids and plunge-frozen using a Leica Electron Microscopy Grid Plunger (Leica Microsystems). Grids were imaged on a CryoARM300 (JEOL) fitted with an in-column Omega filter and K3 camera (Gatan) under low dose conditions.

Physical encapsulation methods of fluorescent protein into caveospheres

Purified fluorescent proteins were mixed with 1 mg/mL of caveospheres and treated with the following physical methods: freeze-thaw (FT) method (liquid nitrogen -196°C for 5 minutes, followed by thawing in an ice bath for 90 minutes over 4 cycles), electroporation (EL) method (2.5 kV, 75 µF, using the Gene Pulser II electroporation system, BIO-RAD) or sonication (SN) method (20% power with 3 seconds on/6 seconds off for 10 cycles using a Qsonica Sonicator Q700, Fisher Scientific). The incubated caveospheres (IN) in each case was an aliquot of the same sample incubated on ice alongside those undergoing encapsulation. Free mScarlet/EGFP proteins after the treatment process were removed using Amicon Ultra Centrifugal Filters- 0.5 100 kDa MWCO (Merck Millipore). The fluorescent signal was then quantitively measured using a microplate reader as caveosphere concentration in the solution was measured by a BCA assay as above.

Acid treatment of EGFP loaded caveospheres

Sonicated EGFP-caveospheres were incubated in citric buffer at decreasing pH levels (6.0, 5.5, 5.0, 4.5) and in PBS 1x (pH 7.4) for 30 min and 1 hour at 37°C. After incubation, the

samples were neutralized with PBS 1x, centrifuged to remove precipitates, and filtered to eliminate fragments. The remaining EGFP-caveospheres were quantified and compared to untreated samples using a BSA assay for caveosphere quantification (as above) and fluorescence measurement with a microplate reader (as above). Western blot analysis was performed against CAV1 using specific antibodies as above.

Fluorescent antibody-labeling of caveospheres

10 µg standard caveospheres were mixed with 0.2 µg of rabbit anti goat- Alexa 488 in 100 µL of PBS 1x and incubated for 1 hour at 37°C. 800 µL of PBS 1x was added to each tube, followed by ultracentrifugation (2 hours, 120,000*g*) and imaged in microcentrifuge tubes as above. Samples were fractionated by sucrose gradients, and fluorescence was quantified using a microplate reader as above. CAV1 content was analyzed using western blotting as above.

To assess the labeling stability on caveosphere, A488-antibody-labeled caveospheres were incubated in DMEM with 10% FBS, 1 % L-glutamine for 72 hours at 37°C. After 72 hours the stability of A488-caveospheres was compared with freshly prepared A488-caveospheres using ultracentrifugation and sucrose gradients as described above. The amount of Alexa 488 fluorescent antibody on the caveosphere was calculated based on their fluorescent signal (λex – 490 nm and λem – 525 nm) determined by a microplate reader and formula described as above.

Loading of DNA, mRNA and DOX into caveosphere using sonication

To label plasmid DNA, SYBR™ Safe DNA Gel Stain (Thermo Fisher Scientific) was added to the plasmid DNA at a dilution of 1:10,000. Excess SYBR was removed with an Amicon Ultra Centrifugal Filter-0.5 100 kDa MWCO (Merck Millipore). The concentration of SYBR-DNA was measured using a microplate reader as described above.

For loading of caveospheres, SYBR-labeled plasmid DNA (1000 ng/µL) was mixed with caveospheres (1 mg/ml) and sonicated termed SYBR-DNA-spheres. To remove unloaded DNA, DNAse 1 was added (179 units at 37 °C for 1 hour), followed by filtration. Mixtures

without sonication and DNA without caveospheres were used as controls. Samples in microcentrifuge tubes were imaged using a ChemiDoc system as above and analyzed via agarose gel electrophoresis. The extent of DNA encapsulation was quantified by treating SYBR-DNA-spheres with Triton X-100 (1% for 1 hour at 37°C) and was measured using a microplate reader as described earlier. mRNA expressing EGFP (BASE mRNA facility, University of Queensland; 300 ng/µL) was mixed with caveospheres (1 mg/ml) sonicated and purified using sucrose gradient described above.

For doxorubin (DOX) loading, caveospheres (1 mg/mL) were mixed with DOX (0.1- 0.5 mg/mL) and sonicated. DOX-caveospheres were treated with Triton X-100 (1% for 1 hour at 37°C) to release DOX, and the loading efficiency was determined using a plate reader as above.

Functionalization of caveospheres for targeting

Fluorescently-labeled caveospheres or cargoes (EGFP, DNA, mRNA, DOX) loaded caveospheres, were functionalized with or without mouse anti-EGFR clone LA 22 at a mass ratio of 50:1. Unbound antibodies were removed using sucrose gradients following the method described earlier.

Cellular uptake of caveospheres

For cellular uptake of caveospheres, cells (A431, HepG2, BEAS-2B) were plated on glass coverslips and cultured overnight until reaching a 60-80% confluence. Anti-EGFR-funtionalized caveospheres (containing A488 antibody or EGFP) prepared at a final concentration of 50 µg/mL were incubated with A431, HepG2 and mixed culture of two cell lines on cover slips for 1 hour at 37°C. SARS-CoV-2-caveospheres (labeled with A488) were incubated with BEAS-2B on over slips for 3 hours at 37°C.

Cell transfection

For cell transfection experiments, caveospheres were loaded with either plasmid DNA encoding EGFP, mRNA encoding EGFP or plasmid DNA encoding diphtheria toxin A (DTA). 150 µg/mL anti-EGFR functionalized DNA/mRNA-caveosphere (containing 687 ng DNA or 299 ng of mRNA) was incubated with the cells (A431, HepG2 and mixed culture) on glass

coverslips or 6 well plates for 1 hour and washed with standard media. Lipofectamine 2000 transfection of EGFP and DTA was conducted as per the manufacturers protocol. The cells were incubated at standard conditions (at 37°C with 5% CO_2) for 24 hours.

For Jurkat cell transfections, 10^6 cells in 500 µL were transfected in a 24 well plate using caveospheres and Lipofectamine as above. An additional spin down protocol using centrifugation (3,000*g*, 5 minutes) was applied for adhesion of cells on coverslips.

After 24 hours, western blotting was performed to evaluate EGFP expression levels in cell lysates collected from each well plate. Expression levels and transfection efficiency were also assessed via confocal microscopy of fixed cell on coverslip described below.

Confocal imaging of fixed cells and Image analysis

For confocal imaging of fixed cells, cells on coverslip were fixed with 4% paraformaldehyde and stained with DAPI. EGF-conjugated Alexa 647 dye at 2 µg/mL was applied to mixed culture. The coverslips then were imaged using a Zeiss LSM880 Fast Airyscan Confocal Microscope. ImageJ software (NIH) was used for flat-field correction of images using the BasiC plugin (Peng et al., 2017). The green fluorescence intensity of 25-35 randomly imaged cells was determined by calculating corrected total cell fluorescence (CTCF) via the equation; CTCF = IntDen − (Area of selected cells X background mean grey value) using ImageJ, where IntDen is "Integrated Density" (Gavet & Pines, 2010; McCloy et al., 2014). From the confocal imaging of fixed cells, total of 90 cells were counted and calculated percentage of EGFP-positive cells for transfection efficiency (%) in A431 cells and Jurkat cell.

CmTT targeted mini screen.

A431 cells in 96 well plates were transfected using 150 µg/mL anti-EGFR functionalized DNA-caveospheres for expressing EGFP and treated with the following reagents: amantadine, azithromycin, chloroquine, dimebon, tamoxifen, amitriptyline, siramesine UNC10217938A (100 µM) and bafilomycin A1 (1µM) for 1.5 hours. Combinatorial treatment with chloroquine and bafilomycin A1 was also conducted. After 1.5 hours, the cells were changed to fresh media and further incubated for a further 24 hours. The expression level of EGFP was

measured from 5-8 wells per samples using a microplate reader at (λex 489 nm, λem 510 nm).

Encapsulated Protein Delivery

50 µg/mL caveospheres loaded with mNG, NLS-mNG, and NLS-7R-mNG plus anti-EGFR antibody were added to A431 cells in an 8-well chamber slide (Nunc™ Lab-Tek™ II CC2™) and incubated at 37°C. Where relevant, chloroquine (100 µM) and bafilomycin A1 (1µM) were added for an hour of incubation. Live cell imaging was conducted on the Zeiss LSM880 Fast Airyscan confocal microscope over 3 hours, capturing 3 random fixed positions in each well at 1, 3-hour time points. ImageJ was used to measure the intensity of green fluorescence in the cell cytoplasm, nucleus and quantified using CTCF quantification in four independent experiments as described above.

DOX-loaded caveosphere experiments.

The DOX, DOX-loaded caveospheres, and DOX-loaded caveospheres plus anti-EGFR antibody at a 2 µg/mL DOX dose were added to A431 cells in an 8-well chamber slide (Nunc™ Lab-Tek™ II CC2™). Live cell imaging was conducted on the Zeiss LSM880 Fast Airyscan confocal microscope over 2 hours, capturing 4 random fixed positions in each well at 0.5-, 1-, and 2-hour time points. ImageJ was used to measure the intensity of green fluorescence in the cell cytoplasm and red fluorescence in nuclei from 15-25 cells at 0.5, 1, and 2 hours, quantified using CTCF quantification in four independent experiments as described above.

Cell viability test

To assess the viability of cells after DTA transfection by caveospheres/Lipofectamine or DOX treatment, the cells at 48 hours incubation time in 96 well plate were treated with PrestoBlue cell viability reagents for 3 hours followed by fluorescence reading using a plate reader (λex – 560 nm and λem – 590 nm). The cell death percentage was calculated based on the fluorescence (subtract background) of treated cell and untreated cells (100% survival baseline). Cell viability after treatment with chloroquine and bafilomycin A1 was performed as above but after 24 hours.

***In vivo* mouse experiments**

Eight-week-old female Balb/c nude Nu/Nu mice were used for *in vivo* targeting experiments. All animal experiments were approved by the University of Queensland's Animal Ethics Committee: Anatomical Biosciences AEC (ABS) committee (Project Number: 2019/AE000105) and the Laboratory Biomedicine AEC - LBM committee (Project Number: 2022/AE000135) and conformed to the guidelines of the Australian Code of Practice for the Care and Use of Animals for Scientific Purposes (AEC approval number: AIBN/CAI/530/15). For all animal models, 8-week-old Balb/c nude mice were acquired from the Animal Resource Centre and were allowed access to food and water *ad libitum* throughout the course of the experiment. Tumors were established by injecting 3×10^6 MDA-MB-468 cells into the left mammary fat pad of anesthetized mice. After 12 days of tumor growth, mice with palpable ~5 mm diameter tumors were selected.

Tumor targeting

For targeting experiments, caveospheres (200 µg) labeled with Alexa 680 secondary antibody with or without anti-EGFR antibody (mass ratio 50:1) were prepared and injected intravenously into the mice's tail veins of the mice. Imaging was performed 24 hours post-injection using an IVIS® Lumina™ X5 imaging system. After imaging, mice were humanely sacrificed, and their organs were imaged ex vivo by an IVIS® Lumina™ X5 imaging system.

Immunofluorescence and western blot of tumor

Tumor samples from above were collected and snap frozen in liquid Nitrogen for Western analysis (as described above), or embedded in O.C.T. Compound (Tissue-Tek®) and frozen in isopentane-cooled liquid nitrogen for histology. For histology analysis, 20 µm cryosections were fixed in 4% PFA, followed by blocking in 2% BSA/PBS 1x. Sections were incubated in primary primary rabbit anti-CAV1 antibody (overnight) and secondary antibodies (1 hour at room temperature) diluted in blocking solution. Images were captured using a Zeiss LSM880 Fast Airyscan Confocal Microscope. For quantification, tissue sections were imaged at three random locations, and mean grey values in the green channel were collected using ImageJ software.

Tumor inhibition

DOX-loaded caveospheres + anti-EGFR were prepared (DOX dose of 4 mg/kg) and administered systemically to mice along with other treatment groups (free DOX, DOX-caveospheres and anti-EGFR functionalized DOX-caveospheres). Each treatment group consisted of 5 mice with 5 injections over 20 days. Tumor growth was monitored using an electronic digital caliper and calculated using the standard volume formula (Pearce et al., 2017; Zhao et al., 2020). Then mice were humanely sacrificed on day 20 and the tumors and hearts were collected (Hather et al., 2014; Zou et al., 2017; Zou et al., 2018). Tumor inhibition rates were calculated on day 20 compared to the control group using this formula: (1 – (mean volume of treated tumors)/(mean volume of control tumors)) × 100%.

Hearts were dissected, fixed in 4% PFA in PBS 1x at 4 °C for 24 hours. Tissue was embedded in paraffin and routine hematoxylin and eosin staining was performed on 10 µm sections by the Queensland Brain Institute histology service at The University of Queensland. Slides were scanned using a Metafer VSlide Scanner by MetaSystems using Zeiss Axio Imager Z2. Images were processed using the QBI Batch SlideCropper and ImageJ. Left ventricular width was calculated using ImageJ.

Software

Figures were prepared using ImageJ and Adobe Illustrator. Schematic images were created with BioRender.com and Microsoft office. Statistics were performed using GraphPad Prism9.

Statistics and replication

Details of all statistical tests, replication and experimental groups are given in the figure legends. In all panels ns: $P > 0.05$, *: $P \leq 0.05$, **: $P \leq 0.01$, ***: $P \leq 0.001$****: $P \leq 0.0001$.

Reagents

Paraformaldehyde (Cat no. P6148-500G, Sigma-Aldrich), Triton X-100 (Cat no. T9284, Sigma-Aldrich), PBS Tablets pH7.2 1000mL/tab.100 tablets (Cat no. 09-9499-10, Astral Scientific), Isopropyl β-D-1-thiogalactopyranoside (IPTG) (Cat no. BIO-37036, Bioline), 4', 6-diamidino-2-phenylindole (DAPI) (Cat no. D9542-5MG, Sigma-Aldrich), Amylose Resin (Cat no. E8021L, Biolabs), TALON® Superflow™ (Cat no. GEHE28-9575-02, Bio-Strategy), Terrific Broth (Cat no. 22711022, Thermo Fisher Scientific), Ampicillin Sodium (Cat no. 016-23301, Novachem), EGF

conjugated Alexa 647 dye (Cat no. E35351, Thermo Fisher Scientific), Doxorubicin hydrochloride injection solution (Cat no. 23214-92-8, Pfizer), SYBR™ Safe DNA Gel Stain (Cat no. Thermo Fisher Scientific), DNAse 1 (Cat no. 18047019, Thermo Fisher Scientific), Lipofectamine 2000 reagent (Cat no. Invitrogen), ECL detection reagent (Life Technologies), BCA protein assay kit (Cat no. 11668019, Thermo Fisher Scientific), Sodium chloride (Cat no. S9888, Sigma-Aldrich), Copper Chloride (Cat no. 222011, Sigma-Aldrich), Sucrose (Cat no. SA030-5KG, Chem-supply), isopentane (Cat no. 270342-1L, Sigma-Aldrich), O.C.T. Compound (Cat no. 4583, Tissue-Tek®). The lysosomotropic agents: Amantadine (A1260), Azithromycin (75199), Chloroquine (C6628), Dimebon (D6196), Tamoxifen (T5648), Amitriptyline (A8404), and Siramesine (SML0976) were from Sigma-Aldrich, while UNC10217938A was from Focus Biosciences (Cat no. HY-136151).

References

Ariotti, N., Hall, Thomas E., Rae, J., Ferguson, C., McMahon, K.-A., Martel, N., Webb, Robyn E., Webb, Richard I., Teasdale, Rohan D., & Parton, Robert G. (2015). Modular Detection of GFP-Labeled Proteins for Rapid Screening by Electron Microscopy in Cells and Organisms. *Developmental Cell*, *35*(4), 513-525. https://doi.org/https://doi.org/10.1016/j.devcel.2015.10.016

Ashfaq, U. A., Javed, T., Rehman, S., Nawaz, Z., & Riazuddin, S. (2011). Lysosomotropic agents as HCV entry inhibitors. *Virology journal*, *8*(1), 163. https://doi.org/10.1186/1743-422X-8-163

Billingsley, M. M., Singh, N., Ravikumar, P., Zhang, R., June, C. H., & Mitchell, M. J. (2020). Ionizable Lipid Nanoparticle-Mediated mRNA Delivery for Human CAR T Cell Engineering. *Nano letters*, *20*(3), 1578-1589. https://doi.org/10.1021/acs.nanolett.9b04246

Brock, D. J., Kondow-McConaghy, H. M., Hager, E. C., & Pellois, J.-P. (2019). Endosomal Escape and Cytosolic Penetration of Macromolecules Mediated by Synthetic Delivery Agents. *Bioconjugate chemistry*, *30*(2), 293-304. https://doi.org/10.1021/acs.bioconjchem.8b00799

Cupic, K. I., Rennick, J. J., Johnston, A. P., & Such, G. K. (2019). Controlling endosomal escape using nanoparticle composition: current progress and future perspectives. *Nanomedicine (Lond)*, *14*(2), 215-223. https://doi.org/10.2217/nnm-2018-0326

Dai, L., Yu, X., Huang, S., Peng, Y., Liu, J., Chen, T., Wang, X., Liu, Q., Zhu, Y., Chen, D., Li, X., Ou, Y., Zou, Y., Pan, Q., & Cao, K. (2021). The therapeutic potential of attenuated diphtheria toxin delivered by an adenovirus vector with survivin promoter on human lung cancer cells. *Cancer Biology & Therapy*, *22*(1), 79-87. https://doi.org/10.1080/15384047.2020.1859870

Fedele, A. O., & Proud, C. G. (2020). Chloroquine and bafilomycin A mimic lysosomal storage disorders and impair mTORC1 signalling. *Biosci Rep*, *40*(4). https://doi.org/10.1042/bsr20200905

Fornari, F. A., Randolph, J. K., Yalowich, J. C., Ritke, M. K., & Gewirtz, D. A. (1994). Interference by doxorubicin with DNA unwinding in MCF-7 breast tumor cells. *Molecular Pharmacology*, *45*(4), 649-656. https://molpharm.aspetjournals.org/content/molpharm/45/4/649.full.pdf

Friedman, A. D., Claypool, S. E., & Liu, R. (2013). The smart targeting of nanoparticles. *Curr Pharm Des*, *19*(35), 6315-6329. https://doi.org/10.2174/13816128113199990375

Gavet, O., & Pines, J. (2010). Progressive Activation of CyclinB1-Cdk1 Coordinates Entry to Mitosis. *Developmental Cell*, *18*(4), 533-543. https://doi.org/https://doi.org/10.1016/j.devcel.2010.02.013

Gilleron, J., Querbes, W., Zeigerer, A., Borodovsky, A., Marsico, G., Schubert, U., Manygoats, K., Seifert, S., Andree, C., & Stöter, M. (2013). Image-based analysis of lipid nanoparticle–mediated siRNA delivery, intracellular trafficking and endosomal escape. *Nature biotechnology*, *31*(7), 638-646.

Hather, G., Liu, R., Bandi, S., Mettetal, J., Manfredi, M., Shyu, W. C., Donelan, J., & Chakravarty, A. (2014). Growth rate analysis and efficient experimental design for tumor xenograft studies. *Cancer Inform*, *13*(Suppl 4), 65-72. https://doi.org/10.4137/cin.S13974

Heath, N., Osteikoetxea, X., de Oliveria, T. M., Lázaro-Ibáñez, E., Shatnyeva, O., Schindler, C., Tigue, N., Mayr, L. M., Dekker, N., Overman, R., & Davies, R. (2019). Endosomal Escape Enhancing Compounds Facilitate Functional Delivery of Extracellular Vesicle Cargo. *Nanomedicine*, *14*(21), 2799-2814. https://doi.org/10.2217/nnm-2019-0061

Kedmi, R., Veiga, N., Ramishetti, S., Goldsmith, M., Rosenblum, D., Dammes, N., Hazan-Halevy, I., Nahary, L., Leviatan-Ben-Arye, S., Harlev, M., Behlke, M., Benhar, I., Lieberman, J., & Peer, D. (2018). A modular platform for targeted RNAi therapeutics. *Nat Nanotechnol*, *13*(3), 214-219. https://doi.org/10.1038/s41565-017-0043-5

Kim, J. S., Choi, D. K., Park, S. W., Shin, S. M., Bae, J., Kim, D. M., Yoo, T. H., & Kim, Y. S. (2015). Quantitative assessment of cellular uptake and cytosolic access of antibody in living cells by an enhanced split GFP complementation assay. *Biochem Biophys Res Commun*, *467*(4), 771-777. https://doi.org/10.1016/j.bbrc.2015.10.066

Klionsky, D., Nyfeler, B., & Murphy, L. (2012). Guidelines for the use and interpretation of assays for monitoring autophagy in higher eukaryotes. *Autophagy*, *8*(4), 445-544.

Krüwel, T., Nevoltris, D., Bode, J., Dullin, C., Baty, D., Chames, P., & Alves, F. (2016). In vivo detection of small tumour lesions by multi-pinhole SPECT applying a 99mTc-labelled nanobody targeting the Epidermal Growth Factor Receptor. *Scientific Reports*, *6*(1), 21834. https://doi.org/10.1038/srep21834

Lu, S., Sung, T., Lin, N., Abraham, R. T., & Jessen, B. A. (2017). Lysosomal adaptation: How cells respond to lysosomotropic compounds. *PLoS One*, *12*(3), e0173771. https://doi.org/10.1371/journal.pone.0173771

McCloy, R. A., Rogers, S., Caldon, C. E., Lorca, T., Castro, A., & Burgess, A. (2014). Partial inhibition of Cdk1 in G2 phase overrides the SAC and decouples mitotic events. *Cell Cycle*, *13*(9), 1400-1412. https://doi.org/10.4161/cc.28401

Momparler, R. L., Karon, M., Siegel, S. E., & Avila, F. (1976). Effect of Adriamycin on DNA, RNA, and Protein Synthesis in Cell-free Systems and Intact Cells1. *Cancer Research*, *36*(8), 2891-2895.

Muro, S. (2012). Challenges in design and characterization of ligand-targeted drug delivery systems. *J Control Release*, *164*(2), 125-137. https://doi.org/10.1016/j.jconrel.2012.05.052

Ntziachristos, V., Bremer, C., & Weissleder, R. (2003). Fluorescence imaging with near-infrared light: new technological advances that enable in vivo molecular imaging. *European radiology*, *13*(1), 195-208.

Pansare, V. J., Hejazi, S., Faenza, W. J., & Prud'homme, R. K. (2012). Review of long-wavelength optical and NIR imaging materials: contrast agents, fluorophores, and multifunctional nano carriers. *Chemistry of materials*, *24*(5), 812-827.

Pearce, A. K., Simpson, J. D., Fletcher, N. L., Houston, Z. H., Fuchs, A. V., Russell, P. J., Whittaker, A. K., & Thurecht, K. J. (2017). Localised delivery of doxorubicin to prostate cancer cells through a PSMA-targeted hyperbranched polymer theranostic. *Biomaterials*, *141*, 330-339. https://doi.org/https://doi.org/10.1016/j.biomaterials.2017.07.004

Peng, T., Thorn, K., Schroeder, T., Wang, L., Theis, F. J., Marr, C., & Navab, N. (2017). A BaSiC tool for background and shading correction of optical microscopy images. *Nature communications*, *8*(1), 14836. https://doi.org/10.1038/ncomms14836

Pinto, I. S., Cordeiro, R. A., & Faneca, H. (2023). Polymer- and lipid-based gene delivery technology for CAR T cell therapy. *Journal of Controlled Release*, *353*, 196-215. https://doi.org/https://doi.org/10.1016/j.jconrel.2022.11.038

Porta, J. C., Han, B., Gulsevin, A., Chung, J. M., Peskova, Y., Connolly, S., McHaourab, H. S., Meiler, J., Karakas, E., Kenworthy, A. K., & Ohi, M. D. (2022). Molecular architecture of the human caveolin-1 complex. *Sci Adv*, *8*(19), eabn7232. https://doi.org/10.1126/sciadv.abn7232

Rahimmanesh, I., Totonchi, M., & Khanahmad, H. (2020). The challenging nature of primary T lymphocytes for transfection: Effect of protamine sulfate on the transfection efficiency of chemical transfection reagents. *Res Pharm Sci*, *15*(5), 437-446. https://doi.org/10.4103/1735-5362.297846

Rosenblum, D., Joshi, N., Tao, W., Karp, J. M., & Peer, D. (2018). Progress and challenges towards targeted delivery of cancer therapeutics. *Nature communications*, *9*(1), 1410.

Rurik, J. G., Tombácz, I., Yadegari, A., Méndez Fernández, P. O., Shewale, S. V., Li, L., Kimura, T., Soliman, O. Y., Papp, T. E., & Tam, Y. K. (2022). CAR T cells produced in vivo to treat cardiac injury. *Science*, *375*(6576), 91-96.

Shi, C., Wu, J. B., & Pan, D. (2016). Review on near-infrared heptamethine cyanine dyes as theranostic agents for tumor imaging, targeting, and photodynamic therapy. *Journal of biomedical optics*, *21*(5), 050901-050901.

Tacar, O., Sriamornsak, P., & Dass, C. R. (2012). Doxorubicin: an update on anticancer molecular action, toxicity and novel drug delivery systems. *Journal of Pharmacy and Pharmacology*, *65*(2), 157-170. https://doi.org/10.1111/j.2042-7158.2012.01567.x

Teo, S. L. Y., Rennick, J. J., Yuen, D., Al-Wassiti, H., Johnston, A. P. R., & Pouton, C. W. (2021). Unravelling cytosolic delivery of cell penetrating peptides with a quantitative endosomal escape assay. *Nat Commun*, *12*(1), 3721. https://doi.org/10.1038/s41467-021-23997-x

Tian, A.-L., Wu, Q., Liu, P., Zhao, L., Martins, I., Kepp, O., Leduc, M., & Kroemer, G. (2021). Lysosomotropic agents including azithromycin, chloroquine and hydroxychloroquine

activate the integrated stress response. *Cell Death & Disease*, *12*(1), 6. https://doi.org/10.1038/s41419-020-03324-w

Walser, P. J., Ariotti, N., Howes, M., Ferguson, C., Webb, R., Schwudke, D., Leneva, N., Cho, K. J., Cooper, L., Rae, J., Floetenmeyer, M., Oorschot, V. M., Skoglund, U., Simons, K., Hancock, J. F., & Parton, R. G. (2012). Constitutive formation of caveolae in a bacterium. *Cell*, *150*(4), 752-763. https://doi.org/10.1016/j.cell.2012.06.042

Yamaizumi, M., Mekada, E., Uchida, T., & Okada, Y. (1978). One molecule of diphtheria toxin fragment A introduced into a cell can kill the cell. *Cell*, *15*(1), 245-250. https://doi.org/10.1016/0092-8674(78)90099-5

Yamamoto, A., Tagawa, Y., Yoshimori, T., Moriyama, Y., Masaki, R., & Tashiro, Y. (1998). Bafilomycin A1 prevents maturation of autophagic vacuoles by inhibiting fusion between autophagosomes and lysosomes in rat hepatoma cell line, H-4-II-E cells. *Cell structure and function*, *23*(1), 33-42.

Yang, B., Ming, X., Cao, C., Laing, B., Yuan, A., Porter, M. A., Hull-Ryde, E. A., Maddry, J., Suto, M., Janzen, W. P., & Juliano, R. L. (2015). High-throughput screening identifies small molecules that enhance the pharmacological effects of oligonucleotides. *Nucleic Acids Res*, *43*(4), 1987-1996. https://doi.org/10.1093/nar/gkv060

Zhao, Y., Fletcher, N. L., Gemmell, A., Houston, Z. H., Howard, C. B., Blakey, I., Liu, T., & Thurecht, K. J. (2020). Investigation of the Therapeutic Potential of a Synergistic Delivery System through Dual Controlled Release of Camptothecin–Doxorubicin [https://doi.org/10.1002/adtp.201900202]. *Advanced Therapeutics*, *3*(6), 1900202. https://doi.org/https://doi.org/10.1002/adtp.201900202

Zou, L., Wang, D., Hu, Y., Fu, C., Li, W., Dai, L., Yang, L., & Zhang, J. (2017). Drug resistance reversal in ovarian cancer cells of paclitaxel and borneol combination therapy mediated by PEG-PAMAM nanoparticles. *Oncotarget*, *8*(36), 60453-60468. https://doi.org/10.18632/oncotarget.19728

Zou, Y., Wei, J., Xia, Y., Meng, F., Yuan, J., & Zhong, Z. (2018). Targeted chemotherapy for subcutaneous and orthotopic non-small cell lung tumors with cyclic RGD-functionalized and disulfide-crosslinked polymersomal doxorubicin. *Signal Transduction and Targeted Therapy*, *3*(1), 32. https://doi.org/10.1038/s41392-018-0032-7

Figure 1: Engineering caveospheres for encapsulation of diverse cargoes and cell-specific targeting:

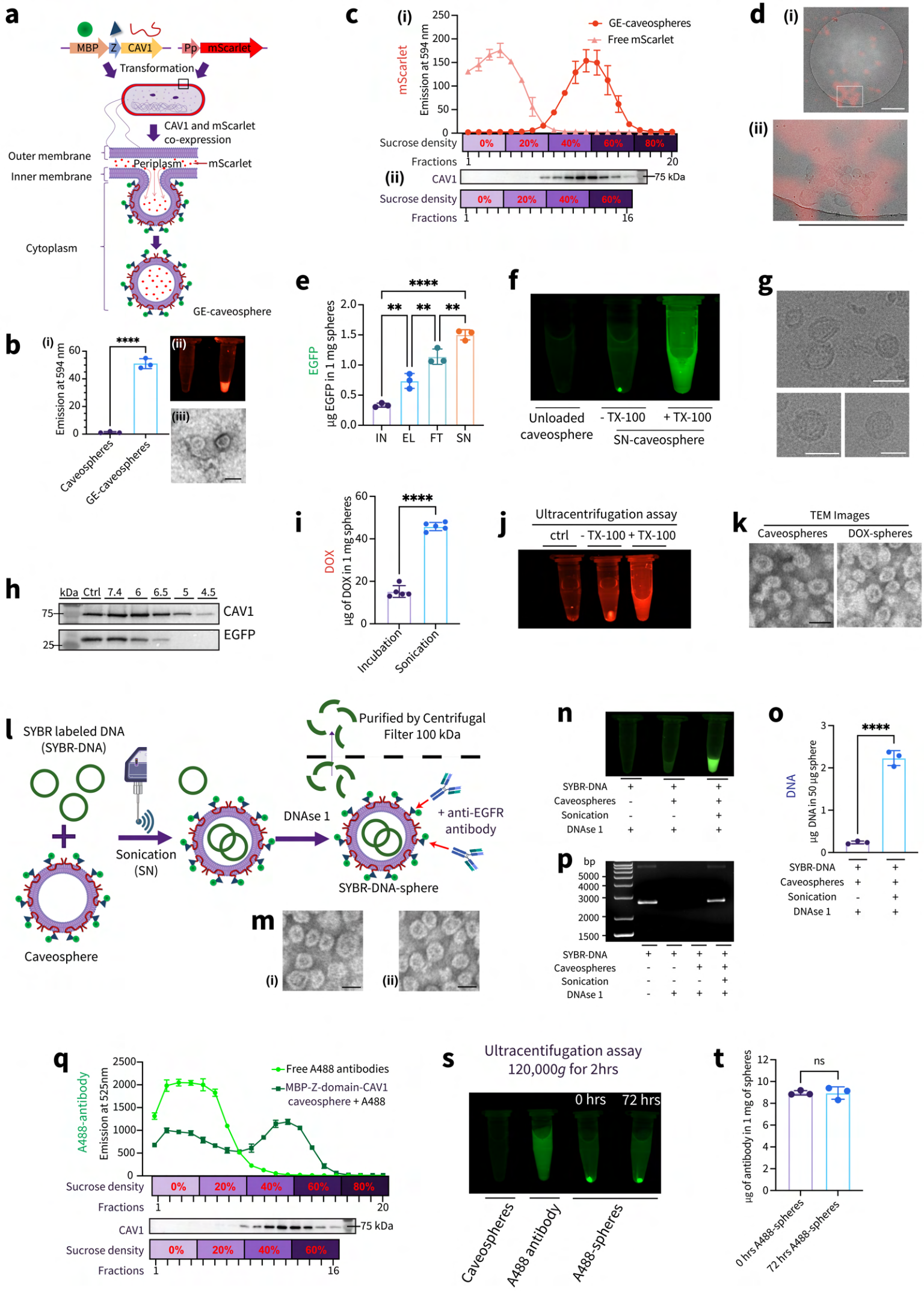

Figure 1: Engineering caveospheres for encapsulation of diverse cargoes and cell-specific targeting:

a, Development of a genetically-encoded method for loading mScarlet into caveospheres using a periplasmic signal peptide in E. coli, termed "GE-caveospheres". **b,** (i) Quantification of fluorescence emission at 594 nm of unloaded caveospheres and GE-caveospheres (n=3 technical replicates, Student's t-test). (ii) Fluorescence emission of unloaded caveospheres (left) and mScarlet-GE-caveospheres (right). (iii) TEM image of GE-caveospheres. Scale bar, 50 nm. **c,** (i) Quantification of fluorescence emission at 594 nm of GE-caveospheres separated by discontinuous sucrose gradient (0%, 20%, 40%, 60%, and 80%, 4 fractions per concentration). Free mScarlet protein was used as a control; n=3 technical replicates. (ii) Western analysis for MBP-Z-domain-CAV1 (72kDa) using anti-CAV1 antibody in fractions collected after a discontinuous sucrose gradient assay of GE-caveospheres (0%, 20%, 40%, and 60%, 4 fractions per concentration). Molecular weight marker (75kDa) as indicated. **d,** (i) Cryo-TEM of mScarlet-GE-caveosphere. (ii) Magnification of boxed area in (i). Scale bars, 500 nm. **e,** Comparison of three physical methods (sonication [SN], electroporation [EL] and freeze-thaw cycling [FT]) for encapsulation of EGFP into caveospheres using fluorescence emission of EGFP-loaded caveospheres (at 507 nm shown as µg protein/mg spheres; n=3 technical replicates, one-way ANOVA, Tukey's multiple comparison test). IN=incubation of proteins and caveospheres without physical treatment. **f,** Fluorescence emission of EGFP-loaded caveospheres, with or without pre-treatment with TX-100 by ultracentrifugation, compared to unloaded caveospheres. **g,** CryoTEM of SN-caveospheres. Scale bar, 50 nm. **h,** Stability of SN-caveospheres (containing EGFP) after incubation at different pH values at 37°C, followed by neutralizing and purification, compared to untreated SN-caveospheres (Ctrl) using Western blot (1 hr pH treatment). **i,** Loading capacity of sonicated DOX-spheres compared to incubation of DOX and caveospheres without sonication expressed as µg of DOX per 1 mg of caveospheres (n=5 technical replicates over two independent experiments, Student's t-test). **j,** Fluorescence emission of DOX-spheres after ultracentrifugation assay in the absence or presence of TX-100, compared to unloaded caveospheres (Ctrl). **k,** Negative stained TEM images of unloaded caveospheres and DOX-spheres. Scale bar, 50 nm. **l,** Schematic for generation of SYBR-labeled DNA (SYBR-DNA) loaded caveospheres by sonication (SYBR-DNA-spheres). SYBR-DNA was loaded into caveospheres via sonication followed by DNAse 1 treatment and centrifugal filtration. SYBR-DNA and SYBR-DNA mixed with caveospheres without sonication, treated with DNase I followed by centrifugal filtration were also included. SYBR-DNA without DNase I treatment was used as a control. **m,** Negative stained TEM images of unloaded caveospheres (i) and SYBR-DNA-spheres (ii). Scale bars, 50 nm. **n,** Fluorescence emission of SYBR-DNA-spheres, SYBR-DNA and SYBR-DNA mixed caveospheres (without sonication) after treatment with DNase 1 and purification. **o,** Loading capability (µg DNA in 50 µg caveosphere) of SYBR-DNA loaded caveospheres with and without sonication using fluorescence emission at 522 nm (n=3 technical replicates, Student's t-test). **p,** Agarose gel electrophoresis of all samples in (n) compared to SYBR-DNA without DNase I treatment. **q,** Fluorescence emission at 525 nm and Western analysis for MBP-Z-domain-CAV1 of fractions collected after sucrose gradient assay of caveospheres + A488 fluorescent antibodybody. Free A488 was used as a negative control. **s, and t,** Stability of MBP-Z-domain-CAV1 caveospheres labeled with A488 (A488-sphere) in a biological medium. Ultracentrifugation assay followed by fluorescence imaging of A488-spheres after 0 hrs (no incubation) and 72 hrs incubation in standard tissue culture media (DMEM/10% FBS) (s). Quantification number of A488 antibody (µg) per caveosphere (mg) after 72 hrs at 37°C in DMEM/10% FBS compared to A488-spheres at 0 hrs using the sucrose gradient ultracentrifugation followed by fluorescence emission at 525 nm of fractions at 40% and 60% sucrose levels (t) (t-test, n=3 technical replicate). **In all panels:** ns: not significant; *: P≤ 0.05; **: P≤ 0.01; ***; P ≤ 0.001****; P≤ 0.0001. Error bars represent mean±SD.

Figure 2: Caveospheres mediate highly specific targeted transfection:

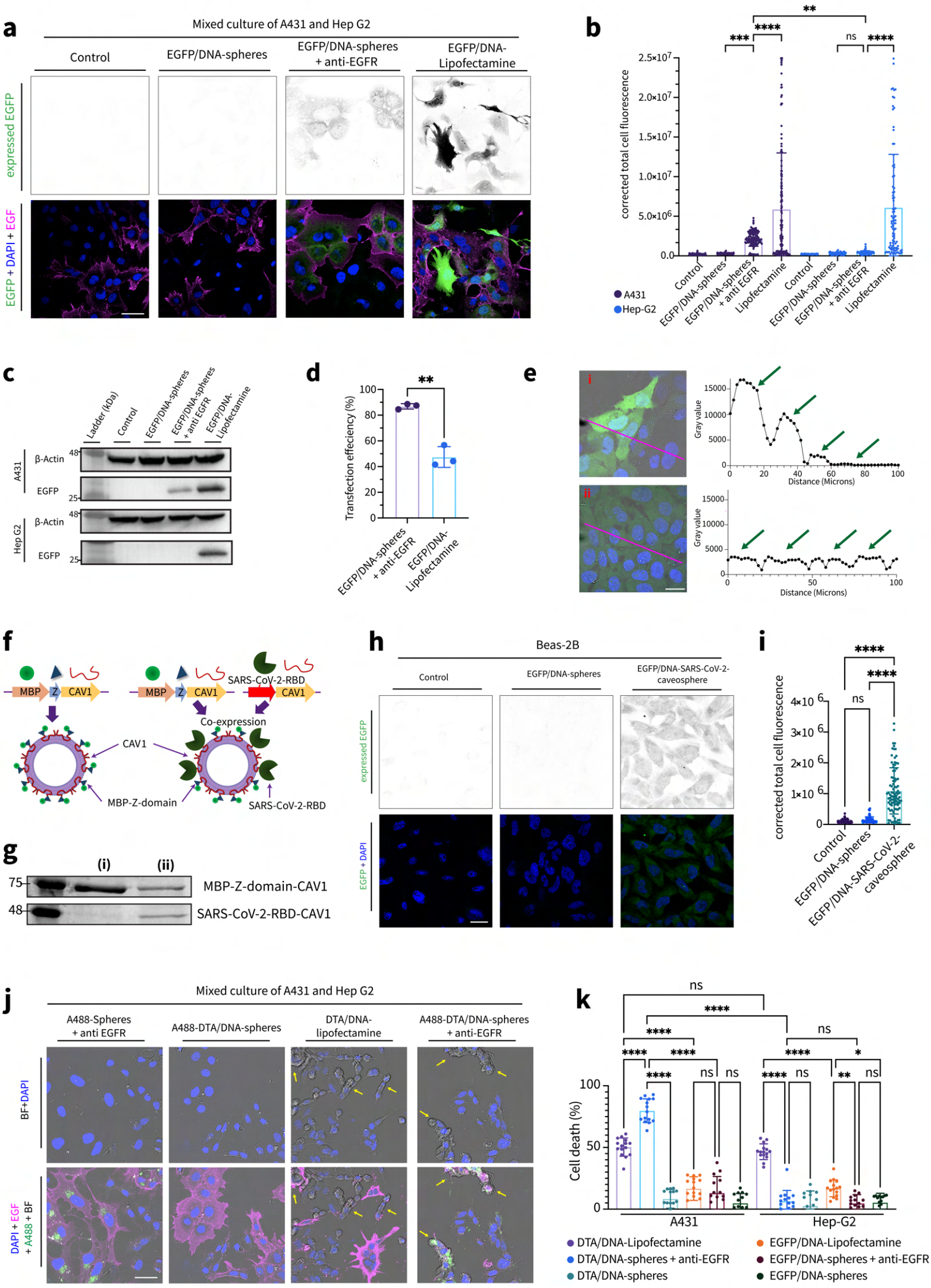

Figure 2: Caveospheres mediate highly specific targeted transfection:

a, Images of EGFP expression (green) in mixed cultures of A431 and HepG2 cells, stained with Alexa647- conjungated EGF (magenta) and DAPI (blue). Cells were untreated (Control), or transfected with EGFP using either DNA-sonicated spheres expressing EGFP (EGFP/DNA-spheres) with and without anti-EGFR functionalization, or using Lipofectamine (EGFP/DNA-Lipofectamine). EGFP expression also shown as inverted images. Scale bar, 40 µm. **b,** Quantification (corrected total cell fluorescence) of EGFP expression in groups shown in (i) (n=3 independent experiments, one-way ANOVA with Tukey's multiple comparison test). **c,** Western analysis of EGFP expression in A431 and Hep G2 cells using EGFP/DNA-spheres +/- anti-EGFR, EGFP/DNA-Lipofectamine, with untreated (Control) cells as a negative control. β-actin is shown as a loading control. **d,** Comparison of transfection efficiency in A431 cells (expressed as percentage of EGFP-positive cells) for EGFP/DNA-spheres + anti-EGFR and EGFP/DNA-Lipofectamine (n=3 independent experiments, student's T-test). **e,** Intensity profile analysis of EGFP expression (gray value) in A431 cells transfected with EGFP/DNA-Lipofectamine (i) or EGFP/DNA-spheres + anti-EGFR (ii). The pixel intensity of EGFP expressed in each cell is indicated by the green arrow. **f,** Schematic for generation of hybrid SARS-CoV-2-caveospheres co-expressing SARS-CoV-2-RBD-CAV1 and MBP-Z-domain-CAV1. **g,** Coomassie-stained SDS-PAGE gel of purified caveospheres (i) and SARS-CoV-2-caveospheres (ii) with bands corresponding to MBP-Z-domain-CAV1 (72 kDa) and SARS-CoV-2-RBD-CAV1 (44 kDa). **h,** Images of EGFP expression in Beas-2B cells after transfection with EGFP/DNA loaded caveospheres, in comparison to EGFP/DNA loaded SARS-CoV-2-caveospheres and untreated (Control) cells, with DAPI staining (blue). Scale bar, 20 µm. EGFP expression shown as grayscale inverted images. **i,** Quantification (corrected total cell fluorescence) of EGFP expression of groups in (f) (n=3 independent experiments, one-way ANOVA with Tukey's multiple comparisons test). **j,** Images of A431 and Hep G2 after 24 hrs incubation with: caveospheres labeled with A488 and anti-EGFR antibodies (A488-spheres + anti-EGFR), DNA expressing DTA loaded caveospheres labeled with A488 antibodies without or with anti-EGFR functionalization (A488-DTA/DNA-spheres and A488-DTA/DNA-spheres + anti-EGFR, respectively), in comparison to DTA transfection with Lipofectamine (DTA/DNA-Lipofectamine). Cells were stained with Alexa647- conjungated EGF (magenta) and DAPI (blue). Deformed cells are highlighted by yellow arrows. Scale bar, 40 µm. **k,** Cell death (%) of A431 and Hep G2 (in different cultures) after 48 hrs transfection with DTA/DNA-sphere, DTA/DNA-sphere + anti-EGFR or DTA/DNA-Lipofectamine calculated based on cell viability assay. The DNA expressing EGFP was used to detect the effect of protein expression in cell proliferation in three conditions as above (EGFP/DNAsphere, EGFP/DNA-sphere + anti-EGFR and EGFP/DNA-Lipofectamine) (n=3 independent experiments, two-way ANOVA with Tukey's multiple comparisons test). **In all panels:** ns: not significant; *: P≤ 0.05; **: P≤ 0.01; ***: P ≤ 0.001; ****: P≤ 0.0001. Error bars represent mean±SD.

Figure 3: Use of caveospheres as a system to study endosomal escape:

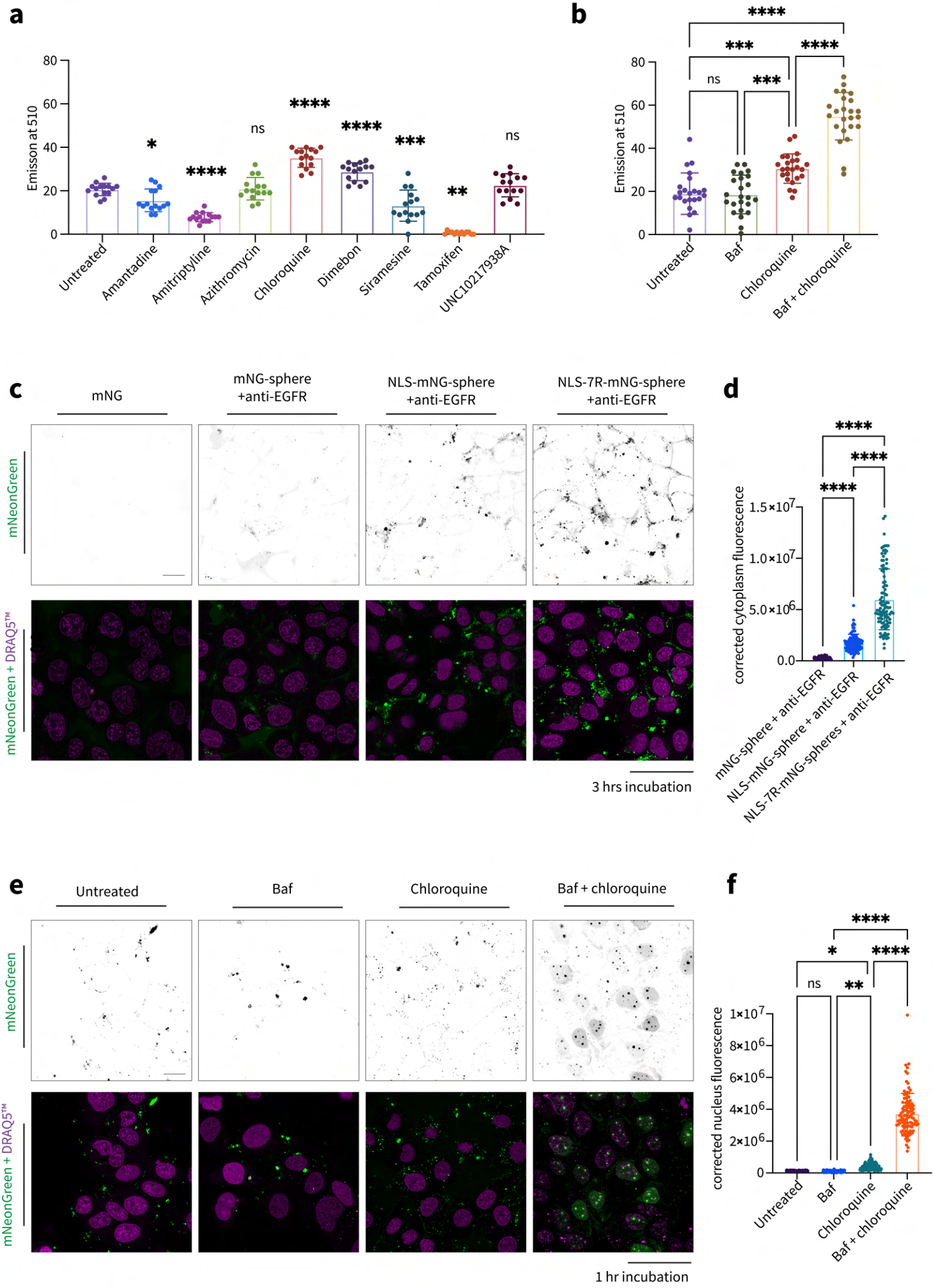

Figure 3: Use of caveospheres as a system to study endosomal escape:

a, Quantification of EGFP intensity in A431 cells transfected with EGFP/DNA-sphere + anti-EGFR and treated with different lysosomotropic agents (n=3 independent experiments, n=5 technical replicates in each experiment, one-way ANOVA with Dunnett's multiple comparisons test between each drug and untreated control). **b,** Quantification of EGFP intensity in A431 cells transfected with EGFP/DNA-sphere + anti-EGFR and treated bafilomycin A1 (Baf), chloroquine, or both Baf+chloroquine (n = 3 independent experiments, n=8 technical replicates in each experiment, one-way ANOVA with Tukey's multiple comparisons tests). Untreated cells were used as a negative control. **c,** Confocal live-cell imaging on A431 cells at 3 hours after incubation with anti-EGFR-functionalized mNG-, NLS- and NLS7R-mNG-spheres, nuclei were stained by DRAQ5™ (magenta pseudo color). Scale bar, 20 µm. mNG shown as grayscale inverted images. **d,** Quantification (corrected cytoplasm fluorescence) of groups in (c) (one-way ANOVA, Tukey's multiple comparisons test, n=3 independent experiments, error bars represent SD). **e,** Confocal live-cell imaging on A431 cells at 1 hour after incubation with anti-EGFR-functionalized NLS-7R-mNG-spheres and treated with Baf, chloroquine, or both, nuclei were stained by DRAQ5™ (magenta pseudo color). Scale bar, 20 µm. mNG shown as inverted grayscale images. **f,** Quantification (corrected nucleus fluorescence) of groups in (e) (one-way ANOVA, Tukey's multiple comparisons test, n=3 independent experiments, error bars represent SD). I**n all panels:** ns: not significant; *: P≤ 0.05; **: P≤ 0.01; ***: P ≤ 0.001; ****: P≤ 0.0001. Error bars represent mean±SD.

Figure 4: Fluorescent antibody labelling caveosphere for *in vivo* trafficking and tumour targeting study in mouse xenograft model:

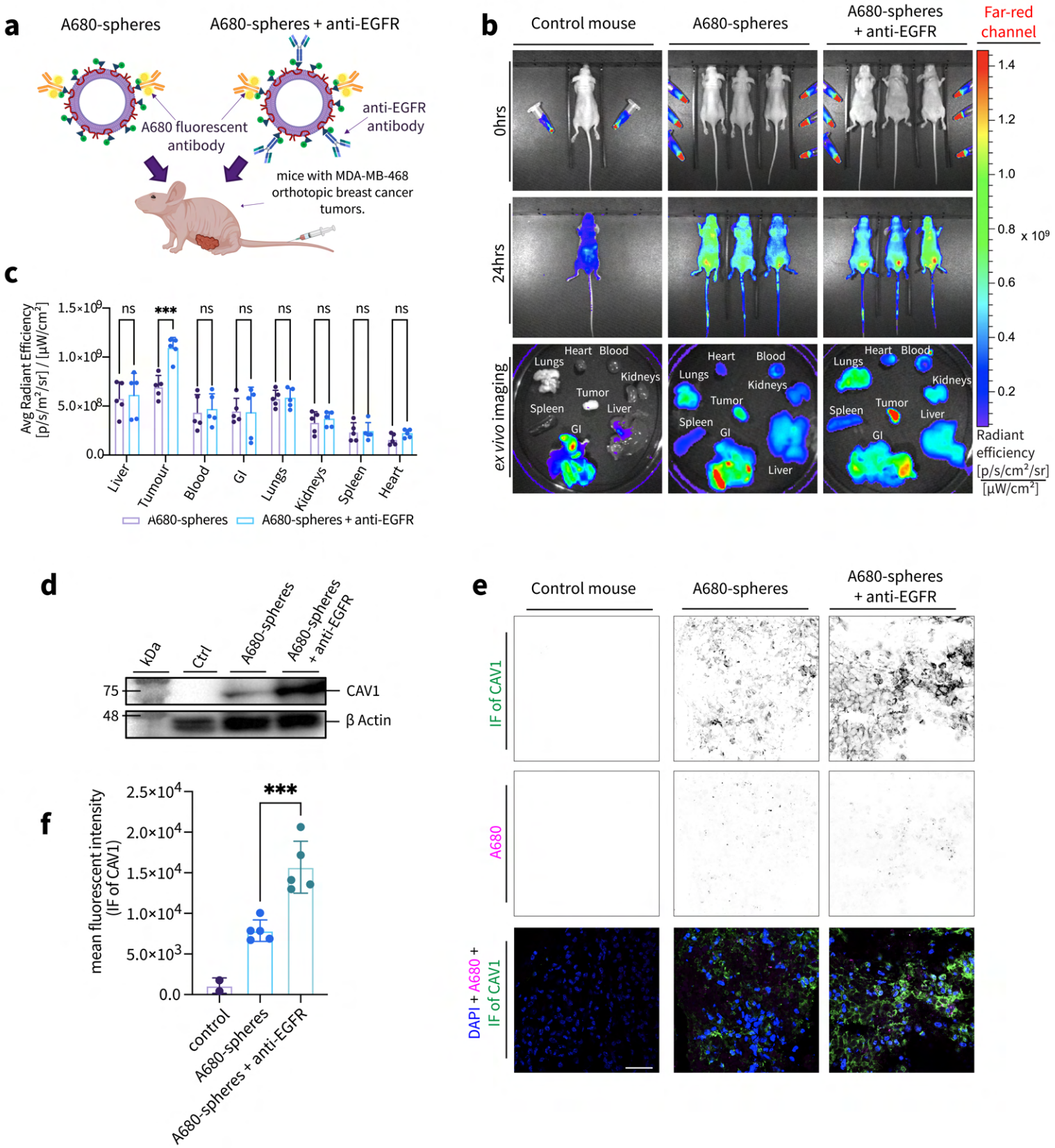

Figure 4: Fluorescent antibody labelling caveosphere for *in vivo* trafficking and tumour targeting study in mouse xenograft model:

a, Schematic for mouse xenograft model of orthotopic breast cancer using caveospheres labeled with Alexa-680 secondary antibody (A680-spheres), and functionalized with anti-EGFR antibody for targeting to the MDA-MB-468 derived xenograft. **b,** *In vivo* imaging of mice injected with control (PBS 1x), A680-spheres or anti-EGFR functionalized A680-spheres (A680-spheres + anti-EGFR). A680 fluorescence shown pre-injection (0 hrs) and 24 hrs post-injection as normalized mean intensity (radiant efficiency) of the near-IR fluorescence is indicated using a blue (low) to red (high) look-up table (n=5 mice per group). *Ex vivo* imaging of A680 fluorescence of tumor, blood, lung, liver, spleen, kidney, gastrointestinal tract (GI) and heart tissues was also performed (one representative mouse shown). **c,** Quantification of average radiant efficiency in the whole tissue regions of all tissues in both A680-spheres and A680-spheres + anti-EGFR cohorts (after subtraction of values from control mice) (n=5 mice per group, two-way ANOVA with Šidák's multiple comparison test). **d,** Western analysis of MBP-Z-domain-CAV1 presented in control, A680-spheres, and A680-spheres + anti-EGFR mouse tumor tissue. β-actin is shown as a loading control. **e,** Images of A680 fluorescence (magenta, inverted images in middle panel) from control, A680-spheres, and A680-spheres + anti-EGFR mouse tumor cryosections, stained with anti-CAV1 antibody (green, inverted images in top panel) and DAPI (blue). Scale bar, 40 μm. **f,** Mean fluorescence intensity of CAV1 in tumor cryosections from control (n=2), A680-spheres (n=5) and A680-spheres + anti-EGFR (n=5) mice (Student's t-test). Dots represent mean intensity of CAV1 imunofluorescence from from 3 randomly selected areas presented in (e). **In all panels:** ns: not significant; *: P≤ 0.05; **: P≤ 0.01; ***; P ≤ 0.001; ****: P≤ 0.0001. Error bars represent mean±SD.

Figure 5: Anti-tumour activity of caveospheres in an *in vivo* model:

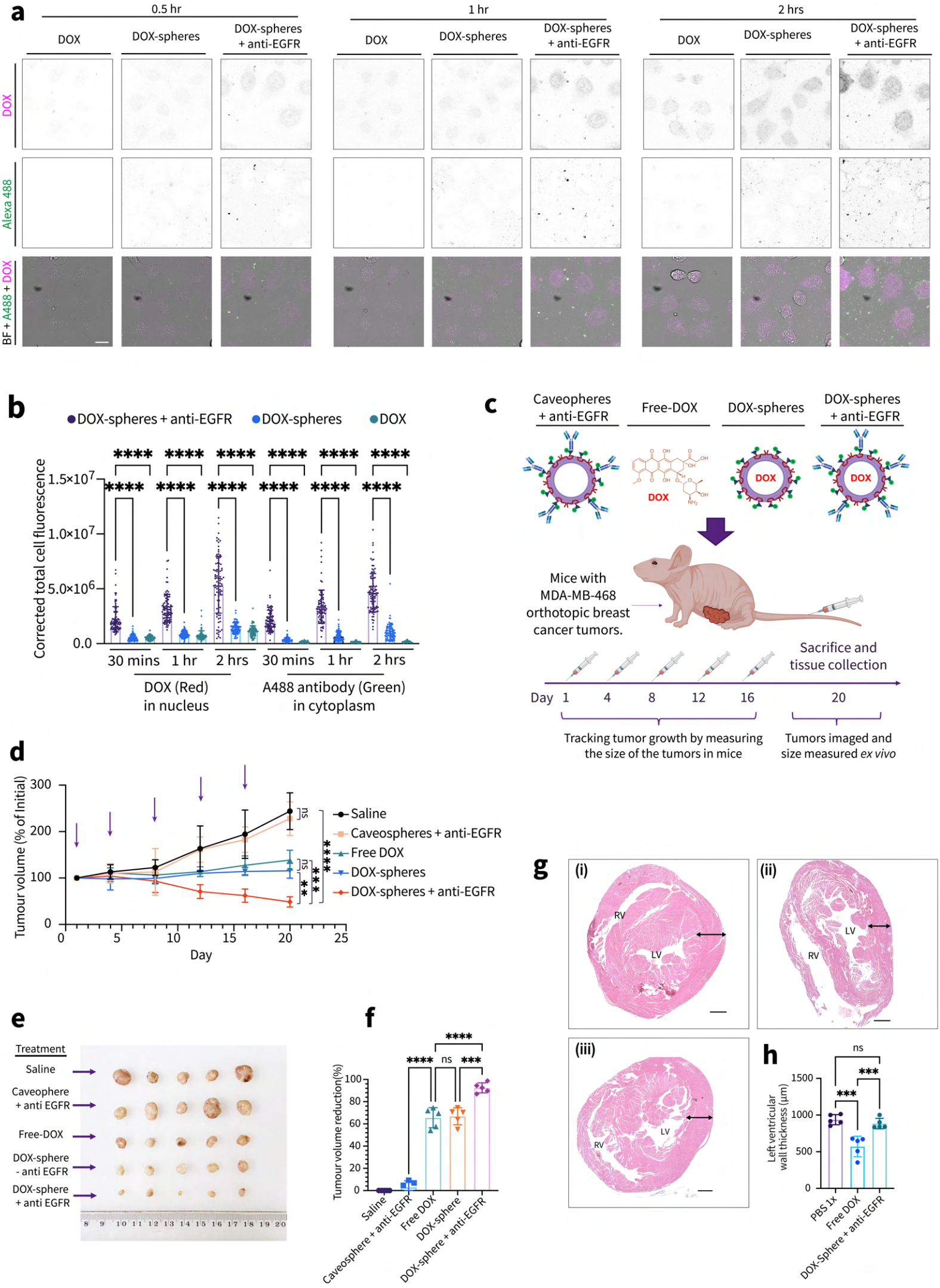

Figure 5: Anti-tumour activity of caveospheres in an *in vivo* model:

a, Live-cell confocal imaging of DOX (magenta) and A488 (green) in A431 cells after incubation with free DOX, A488-DOX-spheres or A488-DOX-spheres+anti-EGFR for 0.5, 1 and 2 hrs. BF, Brightfield. Scale bar, 10 µm. **b,** Quantification (corrected total cell fluorescence) of DOX in nucleus and A488 fluorescence in cytoplasm from live-cell confocal imaging in (f) below (n=4 independent experiments, one-way ANOVA with Tukey's multiple comparisons test). **c,** Schematic of mouse xenograft model of orthotopic breast cancer: Mice were injected with Free DOX, DOX-spheres or DOX-spheres + anti-EGFR on days 1, 4, 8, 12 and 16 of treatment. Saline and anti-EGFR functionalized caveospheres (-DOX) were used as negative controls. **d,** Tumor volumes (expressed a percentage of volume at day 1). Arrows represent days on which mice were dosed. **e,** Excised tumors from mice in (d) after 20 days of treatment. **f,** Tumor inhibition rate (expressed as percentage of reduction in volume compared with saline) in excised tumors after 20 days of treatment. **g,** Representative midventricular cross-section of murine heart from mice in (d) after injection with saline (i), Free DOX (ii) or DOX-spheres + anti-EGFR (iii). Left (LV) and right (RV) ventricles are indicated. Black arrow denotes measurements taken along left myocardium. Tissue was stained with haematoxylin and eosin. Scale bar, 100 µm. **h,** Quantification of left ventricular width from images in (g) (n = 5 mice per group, one-way ANOVA with Tukey's multiple comparison test). For i-h: n=5 mice per group, one-way ANOVA with Tukey's multiple comparisons test. **In all panels:** ns: not significant; *: P≤ 0.05; **: P≤ 0.01; ***: P ≤ 0.001; ****: P≤ 0.0001. Error bars represent mean±SD.

S1

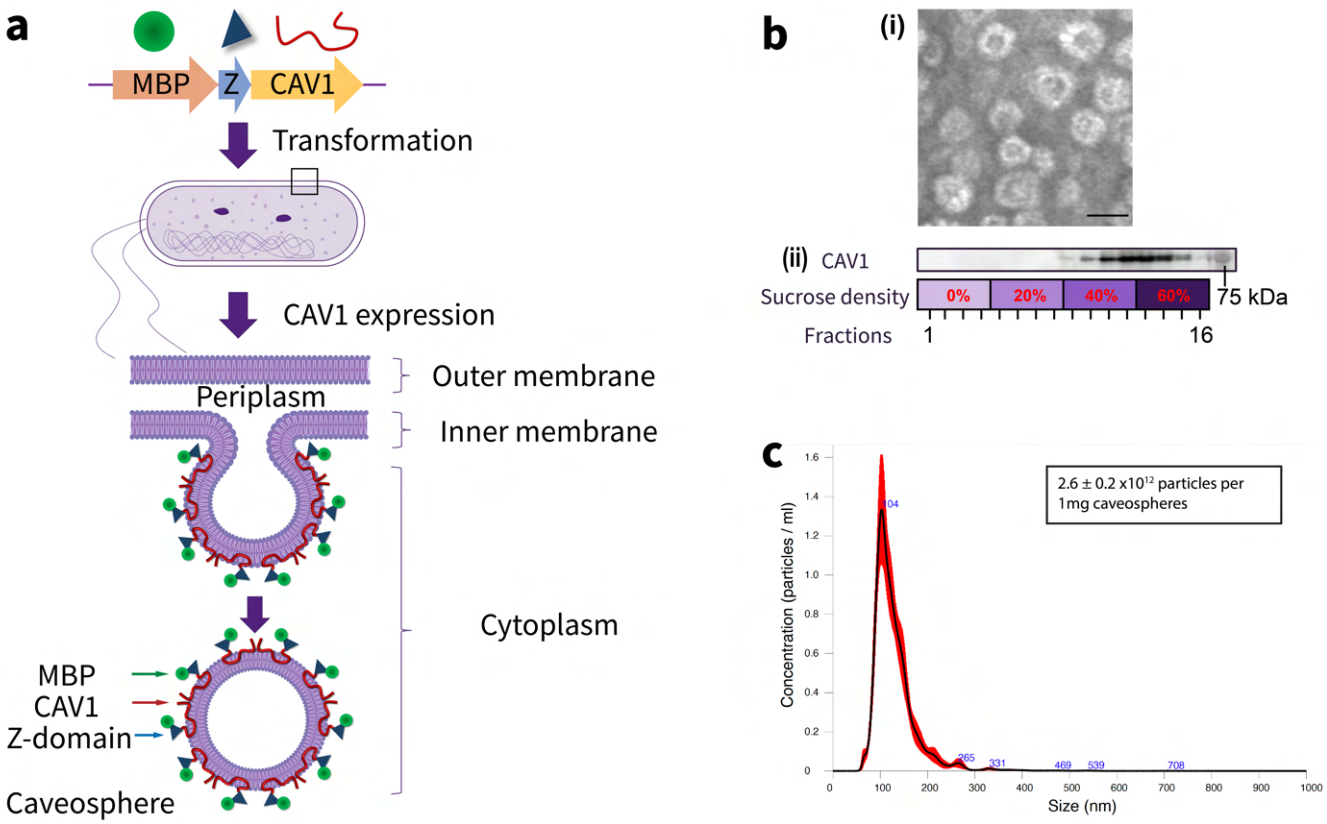

Supplementary Figure 1: a, Caveospheres were formed in E. coli by expression of a fusion protein consisting of Canis lupus familiaris Caveolin1 (CAV1), Maltose-binding protein (MBP) and the Z-domain of protein A (to allow IgG conjugation). Those caveospheres were set as standared caveospheres and used for physical loading cargo, cellular uptake, cell transfection and *in vivo* experiments. **b,** (i) Transmission electron microscopy (TEM) image of caveospheres. Scale bar, 50 nm. (ii) Western analysis for MBP-Z-domain-CAV1 (72kDa) using anti-CAV1 antibody in fractions collected after a discontinuous sucrose gradient assay of caveospheres (0%, 20%, 40%, and 60%, 4 fractions per concentration). Molecular weight marker (75kDa) as indicated. **c,** Nanoparticle tracking analysis report of caveospheres: Finite track length adjustment (FTLA) analysis shows an average caveosphere diameter of 107 ± 4 nm (n = 5 technical replicates, mean - black line, red area - ± SD). Concentration measurements provide an average of particles per 1 mg caveospheres (2 independent experiments, 5 technical replicates per experiment, ± SD)

S2

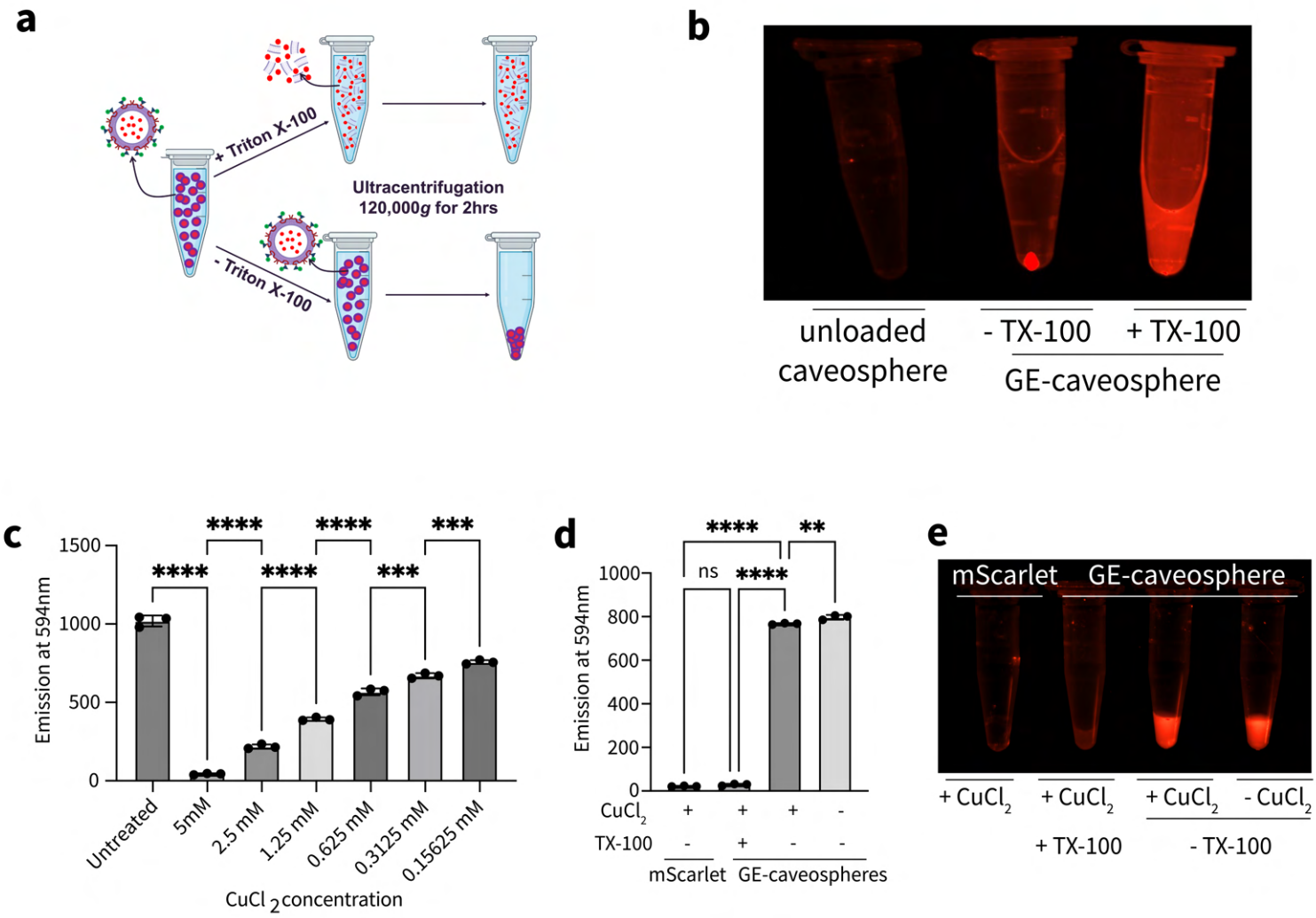

Supplementary Figure 2: a, and b, mScarlet loaded GE-Caveospheres are pelleted by ultracentrifugation at 120,000*g*. Pre-treatment with TritonX-100 (TX-100) detergent to disrupt the caveosphere membrane prevents pelleting. Fluorescence emission of mScarlet encapsulated in GE-caveospheres was then captured using a fluorescent imaging system in (b). **c,** Quantification of mScarlet fluorescence intensity at 594 nm at different $CuCl_2$ concentrations. Concentration of mScarlet protein was 0.1 mg/mL (n=3 technical replicates, one-way ANOVA, Tukey's multiple comparisons test). **d,** Fluorescence intensity at 594 nm of free mScarlet and mScarlet-GE-caveospheres treated with $CuCl_2$ and TX-100 (n=3 technical replicates, one-way ANOVA, Tukey's multiple comparisons test). **e,** Fluorescence emission of free mScarlet and mScarlet-GE-caveospheres treated with $CuCl_2$ and TX-100. **In all panels:** **: P≤ 0.01; ***; P ≤ 0.001****; P≤ 0.0001. Error bars represent mean±SD.

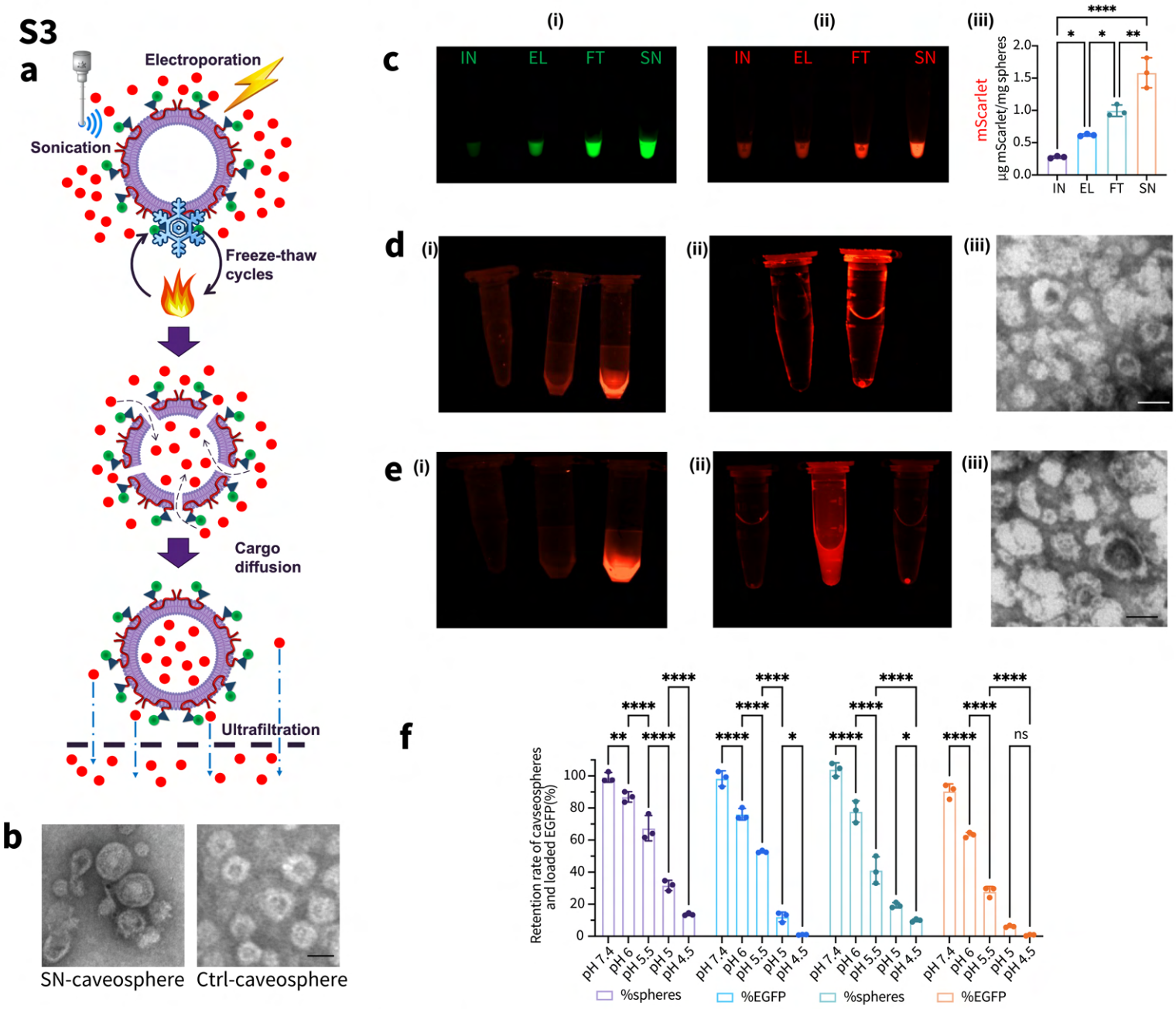

Supplementary Figure 3: a, Schematic diagram of three physical methods used for cargo encapsulation into caveospheres (sonication [SN], electroporation [EL] and freeze-thaw cycling [FT]). **b,** TEM comparison of EGFP-caveospheres loaded by sonication and unloaded caveospheres (Ctrl). **c,** Fluorescence emission of EGFP- and mScarlet-loaded caveospheres in microfuge tubes (i) and (ii) followed by quantification of fluorescence emission of mScarlet-loaded caveospheres by plate-reader (iii). IN=incubation of proteins and caveospheres without physical treatment. **d,** Fluorescence emission of caveospheres after loading with mScarlet by electroporation: (i) fluorescent imaging in the red channel of PBS 1x, unloaded caveospheres and electroporated caveospheres after purification (left to right), (ii) fluorescent imaging in the red channel after ultracentrifugation of unloaded caveospheres (left) and electroporated caveospheres (right), (iii) negative stained TEM image of electroporated spheres. **e,** Fluorescence characteristics of caveospheres after loading mScarlet by freeze-thaw method: (i) fluorescent imaging in the red channel of PBS 1x, unloaded caveospheres and freeze-thawed caveospheres after purification (left to right), (ii) fluorescent imaging in the red channel after ultracentrifugation of unloaded caveospheres, freeze-thawed caveospheres + TX-100 and freeze-thawed caveospheres without TX-100 (left to right) (iii) TEM image of freeze-thawed caveospheres. **f,** Stability of SN-caveospheres (containing EGFP) after incubation at different pH values at 37°C, followed by neutralizing and purification, compared to untreated SN-caveospheres (Ctrl) using BCA protein assay and fluorescence emission of EGFP (30 min and 1 hr pH treatment) for quantification of percentage of EGFP and caveosphere remaining after treatment compared to untreated ctrl as 100% (shown as retention rate, %). **In all panels:** Scale bar, 50 nm. n=3 technical replicates, two-way ANOVA with Tukey's multiple comparisons test, ns: not significant; *: P≤ 0.05; **: P≤ 0.01; ***: P ≤ 0.001; ****: P≤ 0.0001. Error bars represent mean±SD.

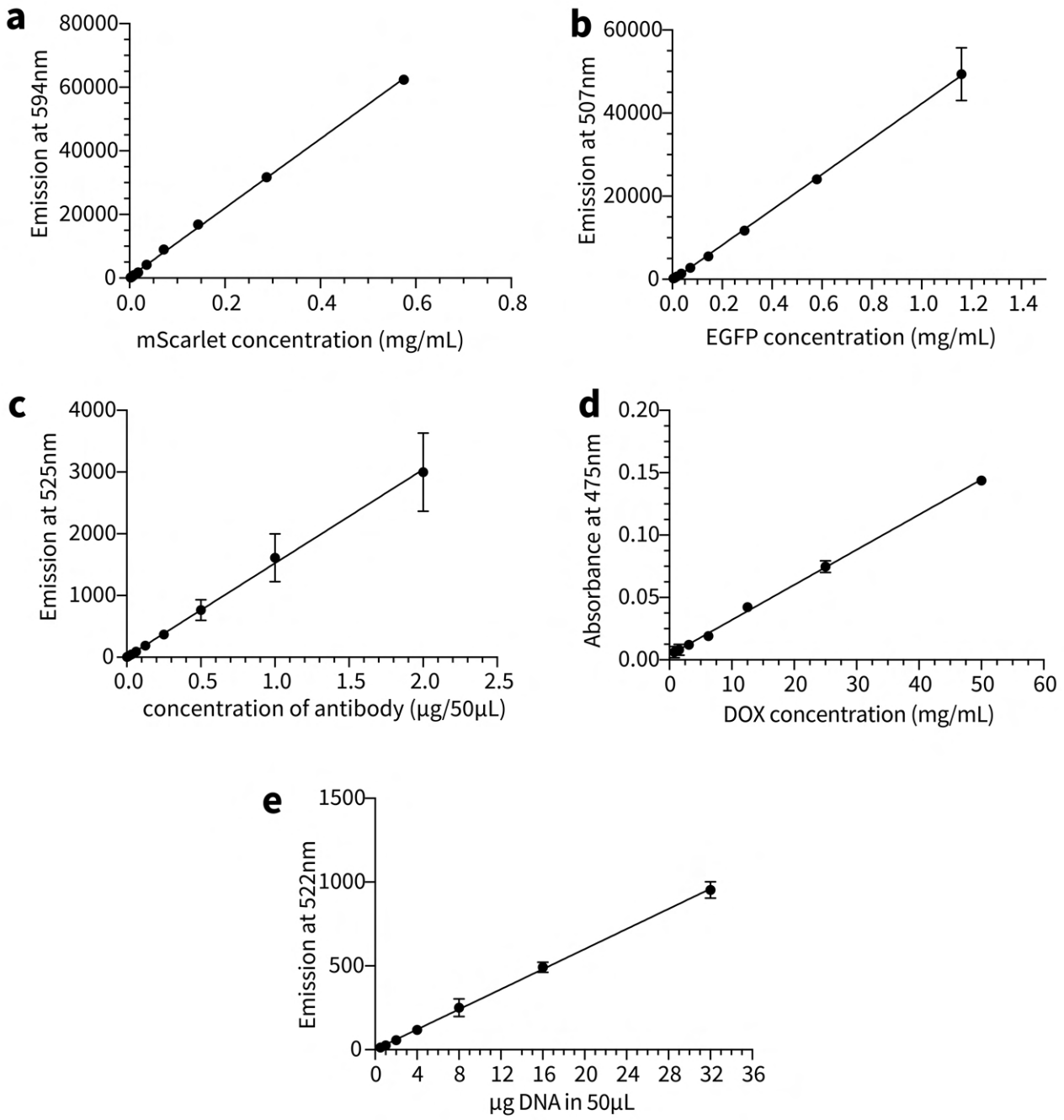

Supplementary Figure 4: a, Linear correlation analysis of mScarlet concentration based on fluorescence emission at 594 nm (n=3 technical replicates). **b,** Linear correlation analysis of EGFP concentration based on fluorescence emission at 507 nm (n=3 technical replicates). **c,** Linear correlation analysis between Alexa-488 fluorescent antibody concentration and fluorescence emission at 525 nm (n=3 technical replicates). **d,** Linear correlation analysis between DOX concentration and absorbance at 475 nm (n=5 technical replicates). **e,** Linear correlation analysis of SYBR-labeled DNA concentration and fluorescence emission at 522 nm. (n=5 technical replicates). **In all panels:** Error bars represent mean±SD.

S5

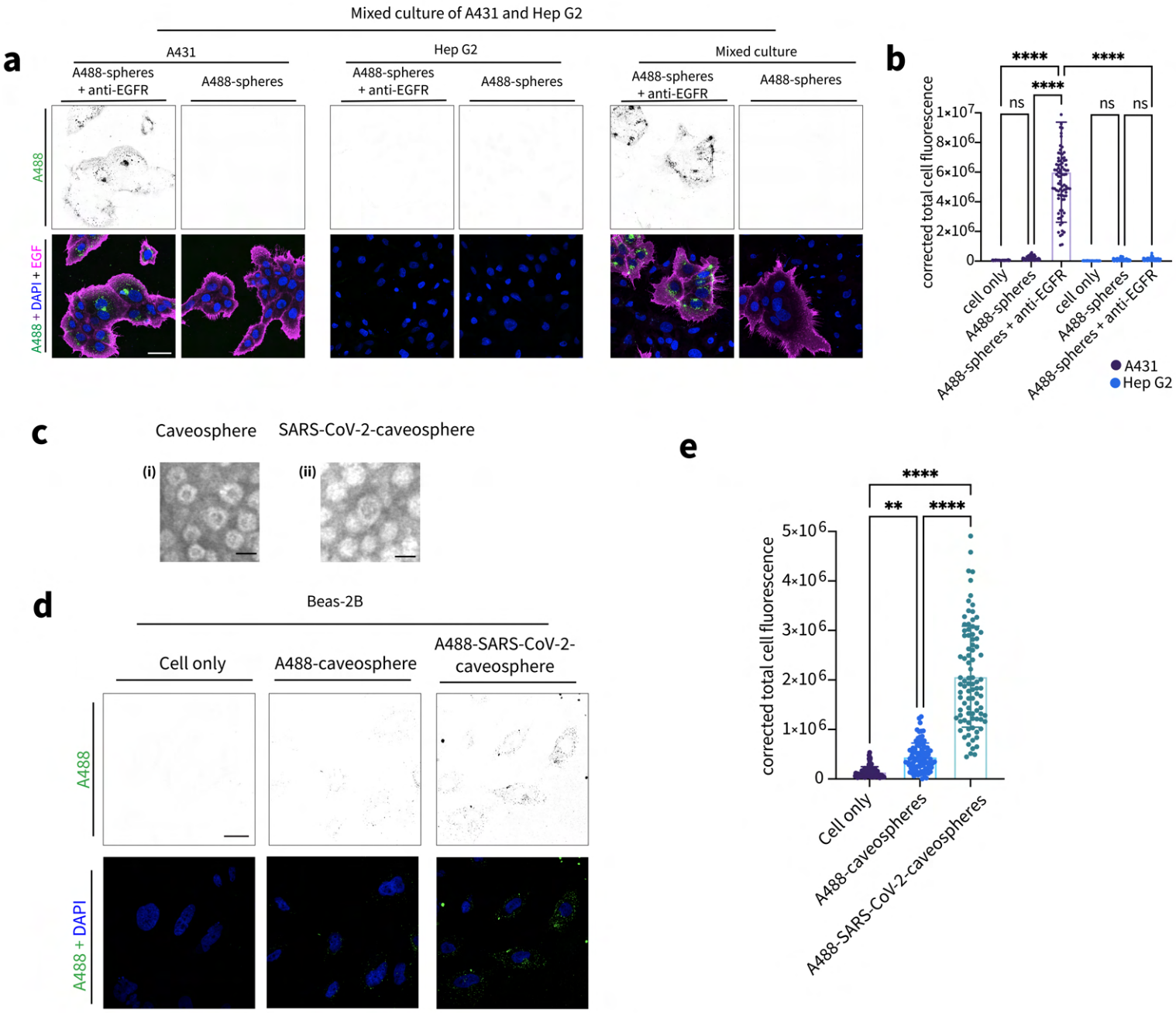

Supplementary Figure 5: a, Images of A431, HepG2 and mixed (A431+HepG2) cells after 1 hr uptake of A488-sphere (green) with and without targeting anti-EGFR antibody, stained with Alexa647-conjungated EGF (magenta) and DAPI (blue channel). A488 fluorescence also shown as inverted images. Scale bar, 40 µm. **b,** Quantification (corrected total cell fluorescence) of A488-sphere fluorescence in A431 and HepG2 cells with and without targeting anti-EGFR antibody (n=3 independent experiments, two-way ANOVA with Tukey's multiple comparisons test). Untreated cells used as a negative control. **c,** TEM image of caveospheres (i) and SARS-CoV-2-caveospheres (ii). Scale bars, 50nm. **d,** Images of A488 fluorescence (green) in Beas-2B cells after 3 hrs uptake of A488-caveospheres and A488-SARS-CoV-2-caveospheres, with DAPI staining (blue). A488 fluorescence also shown as inverted images. Scale bar, 20 µm. **e,** Quantification (corrected total cell fluorescence) of A488 fluorescence in Beas-2Bcells after uptake with A488-caveospheres and A488-SARS-CoV-2-caveospheres groups (n=3 independent experiments, one-way ANOVA with Tukey's multiple comparisons test). **In all panels:** ns: not significant; *: P≤ 0.05; **: P≤ 0.01; ***: P ≤ 0.001; ****: P≤ 0.0001. Error bars represent mean±SD.

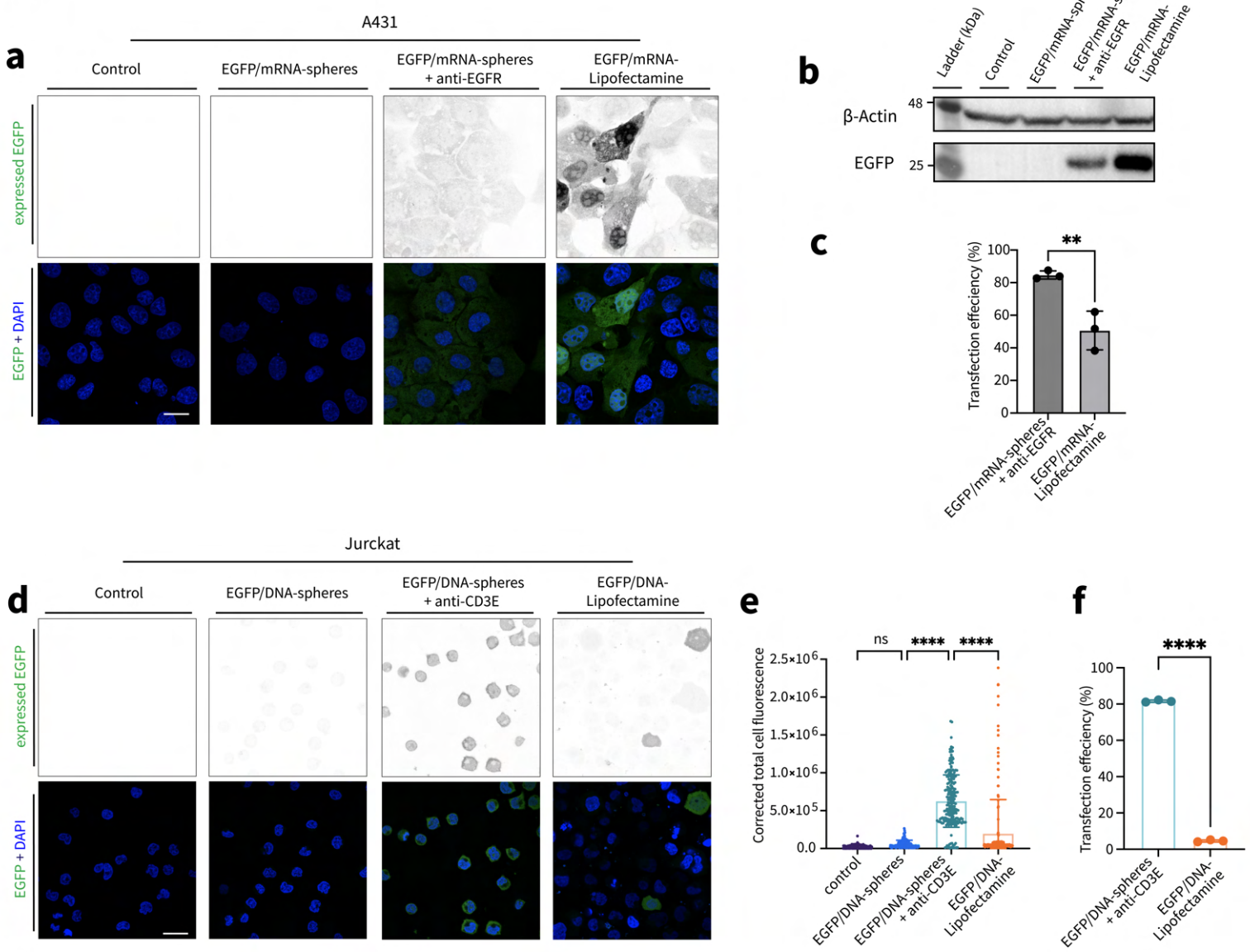

Supplementary Figure 6: a, b and c, A431 cells were transfected with mRNA expressing EGFP loaded caveospheres (EGFP/mRNA-sphere +/- anti-EGFR), in comparison to EGFP/mRNA-Lipofectamine transfection and untreated (Control) cells: Imaging of EGFP expression (green) with DAPI staining (blue) in A431 cells (i). Scale bar, 20 µm. EGFP expression also shown as inverted images. Western analysis of EGFP expression in A431 cells, with β-actin as a loading control (a).a Comparison of transfection efficiency in A431 cells (expressed as percentage of EGFP-positive cells) for EGFP/mRNA-spheres + anti-EGFR and EGFP/mRNA-Lipofectamine (n=3 independent experiments, total of 90 cells counted, student's T-test). **d,** Images of EGFP expression (green) in Jurkat cells after transfection with EGFP/DNA loaded caveospheres (EGFP/DNA-sphere +/- anti-CD3E), in comparison to EGFP/DNA-Lipofectamine transfection and untreated (Control) cells, with DAPI staining (blue). Scale bar, 20 µm. EGFP expression also shown as inverted images. **e,** Quantification (corrected total cell fluorescence) of EGFP expression of groups in (d) (n=3 independent experiments, one-way ANOVA with Tukey's multiple comparisons test). **f,** Comparison of transfection efficiency in Jurkat cells (expressed as percentage of EGFP-positive cells) for EGFP/DNA-sphere + anti-CD3E and EGFP/DNA-Lipofectamine transfection (n=3 independent experiments, student's T-test). **In all panels:** ns: not significant; *: P≤ 0.05; **: P≤ 0.01; ***; P ≤ 0.001****; P≤ 0.0001. Error bars represent mean±SD.

S7

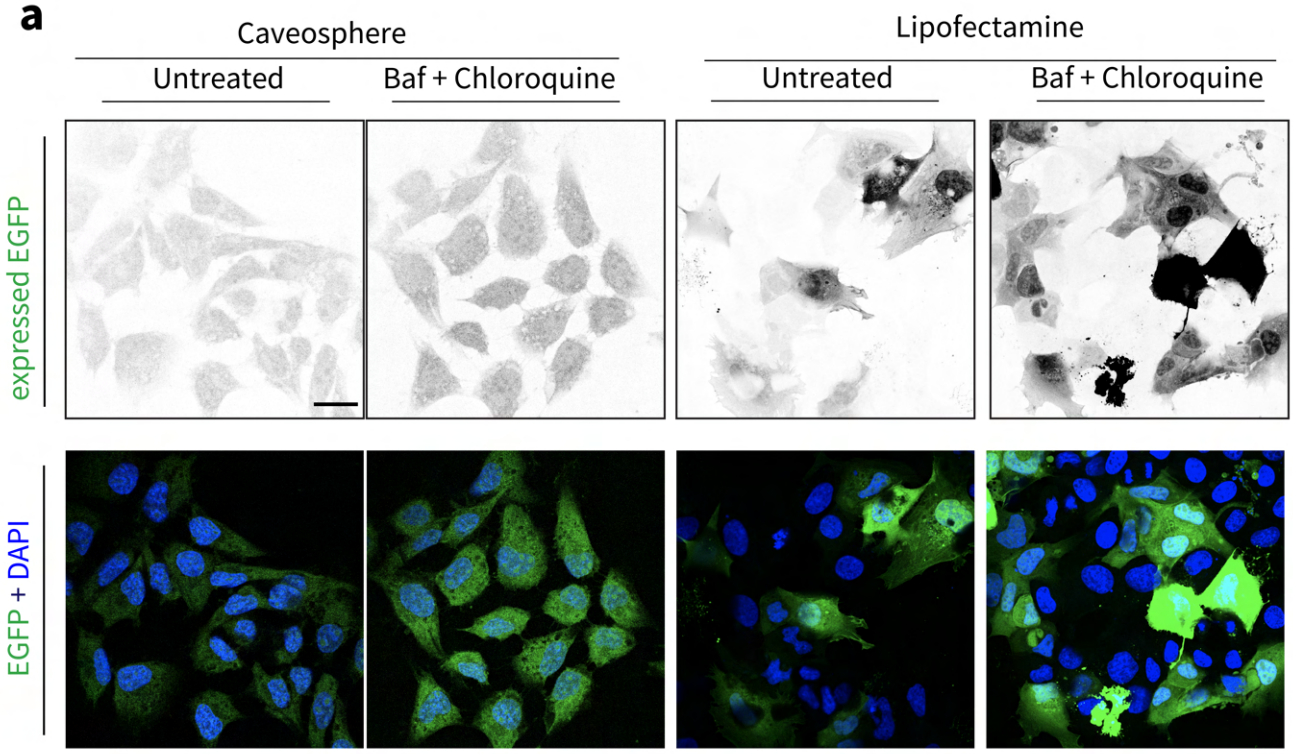

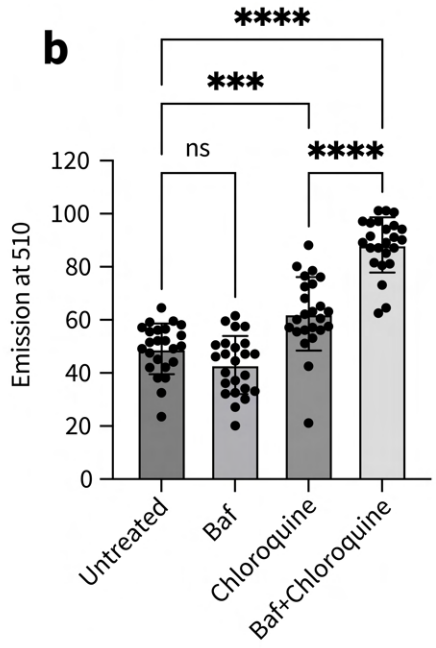

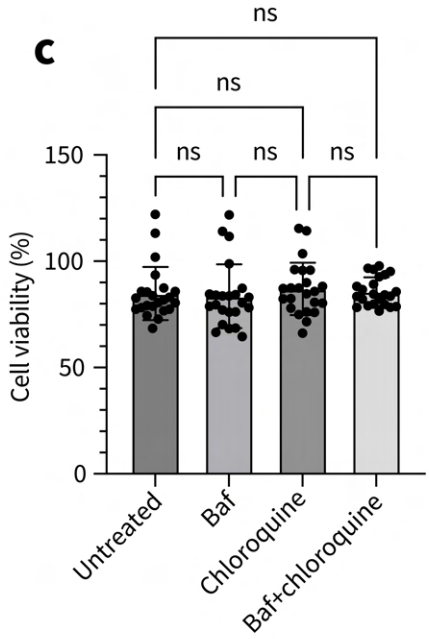

Supplementary Figure 7: a, Caveosphere-mediated targeted transfection (CmTT) using EGFP plasmid. Images of EGFP expression (green) and DAPI staining in A431 cells transfected with EGFP/DNA-spheres + anti-EGFR, followed by treatment with chloroquine and bafilomycin A1. Untreated cells and cells transfected with EGFP/DNA-Lipofectamine included as controls. Images of EGFP expression also shown as inverted images. Scale bar, 20 µm. **b,** Quantification of fluorescence intensity at 510 nm of A431 cells transfected with EGFP using Lipofectamine, followed by treatment with bafilomycin A1 (Baf), chloroquine, or both Baf + chloroquine (n=3 independent experiments, one-way ANOVA with Tukey's multiple comparisons test). Control samples were untreated. **c,** Cell viability (%) of A431 cells after 24 hrs transfected with EGFP/DNA-spheres + anti-EGFR and treatment with Baf, Chloroquine, or both Baf and Chloroquine, compared to untreated control (n = 3 independent experiments, one-way ANOVA with Tukey's multiple comparisons test). Control samples were untreated). **In all panels:** ns: not significant; ***: P ≤ 0.001; ****: P≤ 0.0001. Error bars represent mean±SD.

S8

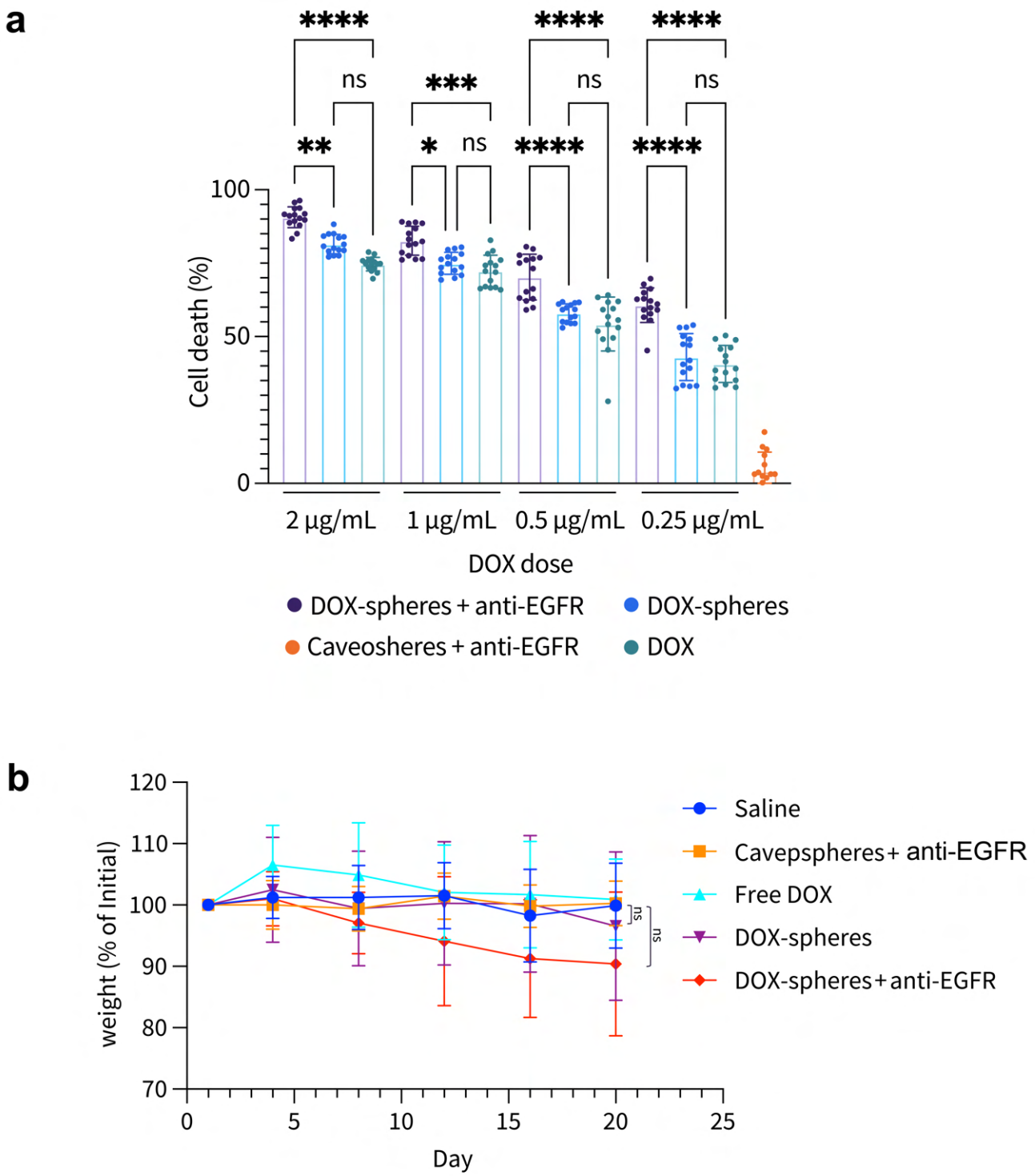

Supplementary Figure 8: a, Cell death (%) calculated based on cell viability assay of A431 cells after 48 hrs treatment with DOX-spheres + anti-EGFR, DOX-spheres or free DOX (n=3 independent experiments, two-way ANOVA with Tukey's multiple comparisons test). Untreated cells were set as the 100% survival baseline. **b,** Weight of mice (expressed as a percentage of starting weight at day 1) following a tumor regression study over 20 days (n=5 mice per treatment, one-way ANOVA with Tukey's multiple comparisons test, error bars represent SD). Mice were injected with Free DOX, DOX-spheres or DOX-spheres + anti-EGFR on days 1, 4, 8, 12 and 16 of treatment. Saline and anti-EGFR functionalized caveospheres (-DOX) were used as negative controls. **In all panels:** ns: not significant; *: P≤ 0.05, **: P≤ 0.01, ***: P ≤ 0.001, ****: P≤ 0.0001. Error bars represent mean±SD.

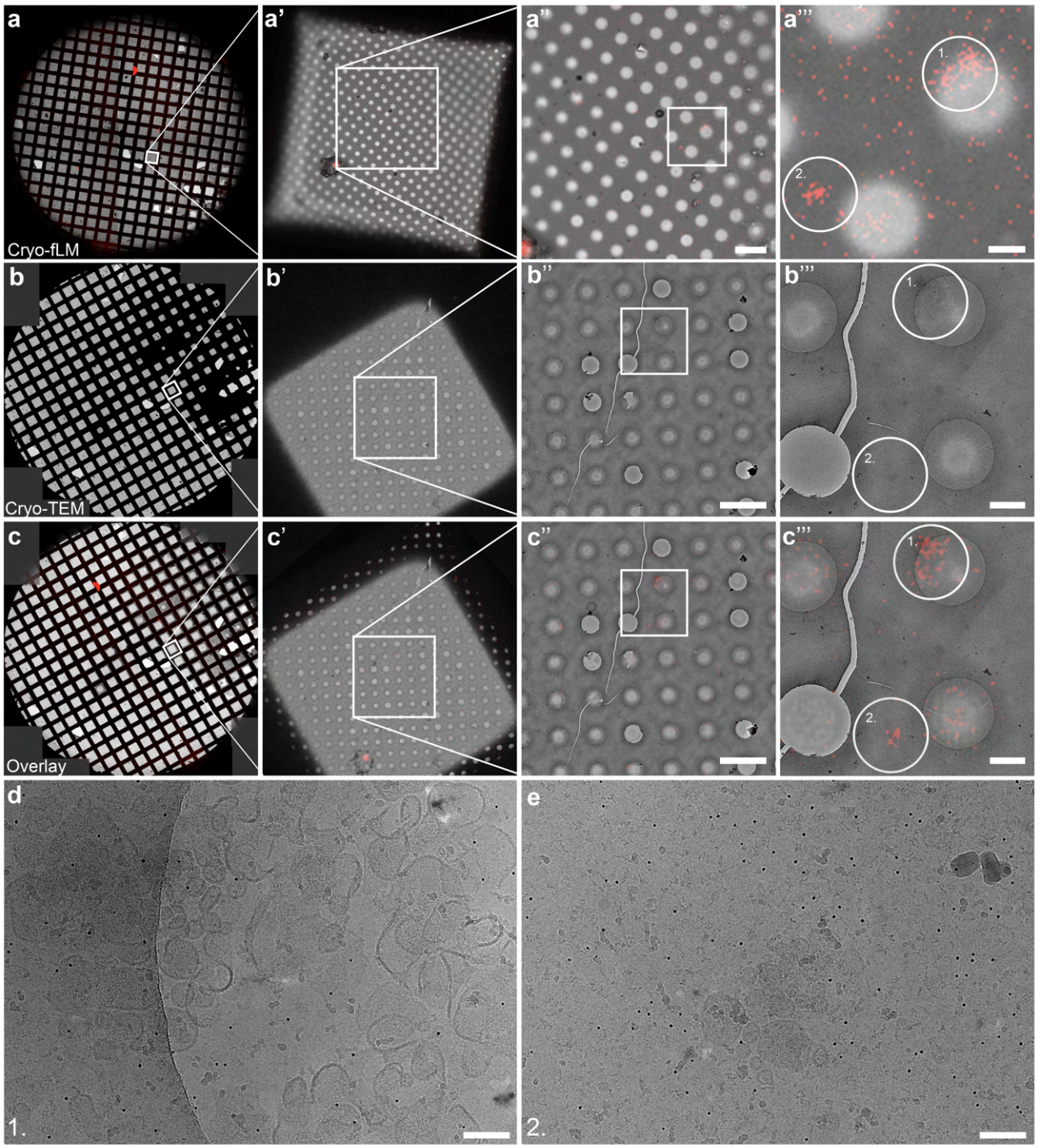

Supplementary Figure 9: Validation of the cryo-CLEM approach with additional areas of interest (related to Figure 1h). mScarlet periplasmic expression results in encapsulation of fluorescence within heterologous caveolae. Cryo-fluorescence light microscopy of additional regions of interest shows striking co-localization between mScarlet fluorescence intensity and caveospheres. **a-a'''**, Low magnification brightfield with cryo-confocal detection of the mScarlet signal showing low magnification whole grid (a), to grid square level (a'), to region (a''), to hole (a''') tracking of mScarlet signal. **b-b'''**, Cryo-EM of detection of the same grid and regions from (a). **c-c'''**, Overlay of cryo-fluorescence image from (a) with cryo-EM image from (b) demonstrating grid fitting (c), to grid square level (c'), to region (c''), to hole detection (c''') tracking results in the agreement of morphologically definable caveospheres at sites of enriched mScarlet signal. Region 1 and Region 2 are highlighted. **d**, ,High-magnification of cryo-electron micrograph of region 1 (from a''', b''' and c''') shows clustered caveospheres at the area of enriched mScarlet fluorescence. **e**, High-magnification of cryo-electron micrograph of region 2 (from a''', b''' and c''') shows clustered caveospheres at the area of enriched mScarlet fluorescence. Scale bars: 5µm in a'', b'' and c''; 1µm in a''', b''' and c '''; 100 nm in d and e.

Supplementary 10: Caveats

The caveosphere system relies on generation of caveolin-containing vesicles in bacteria. While host proteins are largely excluded from the forming caveospheres (Walser et al, 2012), even highly purified caveosphere preparations will harbor host endotoxins such as LPS with biomedical complications. Although caveospheres did not exhibit toxicity in the A431 and Hep-G2 cell lines, the LPS was reported link to inflammatory cytokine production, and to cell death via apoptosis of macrophages (Xaus et al., 2000) and monocytes (Monguió-Tortajada et al., 2018). Thus, while the caveosphere system offers a powerful modular system to understand and optimize delivery to specific cells and cellular compartments in cell culture (CmTT method) and *in vivo*, further refinement would be required to render caveospheres suitable for biomedical applications.